Engineering Structures 155 (2018) 73–90

Contents lists available at ScienceDirect

Engineering Structures

journal homepage: www.elsevier.com/locate/engstruct

A composite beam theory for modeling nonlinear shear behavior

Fang Jiang*[1], Ankit Deo[2], Wenbin Yu[3]

Purdue University, West Lafayette, IN 47907-2045, USA

ARTICLE INFO

Keywords:
Composite beam
Nonlinear constitutive law
Free-edge effect
Laminate
Variational asymptotic method
VABS

ABSTRACT

Accurate predictions of physically nonlinear elastic behaviors of a material point in the structure are essential to the further analyses which are beyond the linear elasticity regime, for example, the progressive damage and the failure. In light of substantial experimental evidence of nonlinear shear stress-strain responses in composites, it is necessary to consider them in the structure-level simulations rigorously. A variational asymptotic beam model is developed for this purpose. The three-dimensional continuum is rigorously reduced to a two-dimensional cross-sectional analysis and a one-dimensional Euler-Bernoulli beam analysis. The original three-dimensional continuum features material nonlinearities in longitudinal shear. The unknown cross-sectional warping is solved by finite element method using the principle of virtual work. Nonlinear beam constitutive relation and three-dimensional stress and strain fields are obtained.

1. Introduction

Fiber-reinforced plastic composites (FRP) exhibit physically nonlinear behaviors in both elastic and inelastic regions. The primary cause of the elastic nonlinearity has been discovered to be the lamina shear stresses once they are relatively large compared to the longitudinal tensile stresses. In this situation, the resin matrix dominates in the mechanical performance of the composites. Consequently, because the shear stress-strain responses of polymer resins are nonlinear over the entire strain range and at very low strain levels, the in-plane shear responses of FRP plies are nonlinear over the entire range examined [1].

Several mathematical models have been published to describe the nonlinear stress-strain responses. A widely used example of these models are developed by Hahn and Tsai [2] by employing a plane-stress complementary energy function which contains a biquadratic term for in-plane shear stress. Stress field predicted by such a constitutive law is used to formulate the failure criterions which are successful in predicting the failure due to stress concentrations [3,4]. Another widely used model is the Ramberg-Osgood equation [5] which is also popular in metal fatigue studies. A more flexible description methodology is to utilize mathematical curve fitting functions [6–8]. A comprehensive review of the nonlinear constitutive models for shear nonlinearity can be found in [9].

The focus of this paper is not to just provide another method to describe the nonlinear shear stress-strain law but to bridge the theoretical gap between the physically nonlinear laws and the mechanics of slender solid made of the materials which are governed by these laws. We have two main motivations for this study. Firstly, the knowledge of the nonlinear shear stress-strain response of the composites can be obtained from the measurements of loaded slender coupons. For example, the ASTM D3518/D3518M Standard Test Method [10] for "in-plane shear response of polymer matrix composite materials by the tensile test of ± 45° laminate" is based on the measured uniaxial force-strain response of a symmetrically ± 45°-laminated coupon. A rigorous beam model can serve as a virtual coupon to relate the uniaxial force-strain response precisely with the three-dimensional (3D) stress and strain fields by the cross-sectional analysis. Consequently, the beam model can be used along with the data matching tools to calibrate the material constants built into the material descriptions. Secondly, the nonlinear in-plane shear responses have impacts on the one-dimensional (1D) constitutive responses of beams. Predictions of static failure loads and natural frequencies of composite beams are affected by the predefined 3D nonlinear stress-strain laws.

A substantial amount of work has been devoted to model composite beams. The conventional beam theories adopt the ad hoc assumptions, for example, the cross section remains rigid in its own plane and possesses uniaxial stress state, have limited their generality and accuracy in predicting the behavior of composite beams. An advanced theory should be free from the limitation of unnecessary kinematic assumptions and minimize the information loss from the original 3D model.

* Corresponding author.
E-mail address: f.fang.jiang@gmail.com (F. Jiang).
[1] Graduate Research Assistant, School of Aeronautics and Astronautics. Currently, Engineer at the Cooper Tire and Rubber Company.
[2] Graduate Research Assistant, School of Aeronautics and Astronautics.
[3] Professor, School of Aeronautics and Astronautics.

https://doi.org/10.1016/j.engstruct.2017.10.051
Received 13 April 2017; Received in revised form 18 September 2017; Accepted 19 October 2017

The variable kinematic model, known as the Carrera Unified Formulation (CUF) [11], permits one to develop a structural model with a variable number of displacement unknowns in a hierarchical manner. Another systematic approach for modeling composite beams has been developed by Hodges and his co-workers during the last three decades [12–17]. This approach uses the Variational Asymptotic Method (VAM) [18] to rigorously split the original 3D geometrically nonlinear and materially linear problem of the slender structure into a 1D global beam analysis and a two-dimensional (2D) cross-sectional analysis. The 2D cross-sectional analysis is called Variational Asymptotic Beam Sectional Analysis (VABS). The advantageous feature of this approach is that the resulting beam models are still in the form of simple engineering models such as the Euler-Bernoulli beam model or the Timoshenko beam model without the ad hoc assumptions such as that the plane cross section remains plane associated with these models. VABS provides the constitutive relations needed for the global 1D beam analysis and computes the pointwise fields (such as stress and strain) within the original 3D structure based on the global beam behavior. The nonlinear elasticity is studied in VABS framework firstly by assuming nonlinear strain definition (Green strain in St-Venant/Kirchoff model) to examine the trapeze effect for strip-like beams [19]. Jiang, Yu, and Hodges extended the VABS theory to deal with various types of hyperelastic material both analytically [20] and numerically [21]. The motivations to use VABS instead of 3D FEA is the computational efficiency, numerical stability, coupon constitutive relation representative, and flexibility for complex composite mold profile.

In the present work, VABS is extended to model the physically nonlinear beams. In light of releasing the small warping assumption to the finite warping, the nonlinear product terms of the warping and curvatures are retained in the strain formulation. The theoretical foundation of VABS is updated from minimizing the strain energy to the principle of virtual work. Newton-Raphson method is utilized to solve for the converged warping solution iteratively.

The Hahn-Tsai [2] nonlinear in-plane shear model is used for validation purpose by comparing the VABS results with those from 3D FEA. Both static and dynamic examples are given. The ± 45°-laminated coupon tensile tests are simulated. 3D local fields such as the free-edge stresses are precisely captured by the present model. Nominal stress-strain curves predicted for various composite beams with different cross-sections are compared to show the impact of the cross-sectional designs of the coupons on their performances in calibrating the material constants.

2. Variational asymptotic beam sectional analysis (VABS)

2.1. Theoretical formulation

In Fig. 1, $\boldsymbol{e}_i$ for $i = 1, 2, 3$ are fixed dextral, mutually perpendicular unit vectors in the absolute reference frame, and $\boldsymbol{r}_0$ and $\boldsymbol{R}_0$ denote the position vector of the material point on the reference line of the undeformed and deformed configurations, respectively. $\boldsymbol{b}_i$ and $\boldsymbol{B}_i$ are the orthogonal triads attached to the cross-section in the undeformed and deformed configurations, respectively. Here and through all the paper, expect where explicitly indicated, Greek index α assumes values 2 and 3, whereas Latin indices (i, j, k, l, m, n, p, and q) assume values 1, 2, and 3. Repeated indices are summed over their range except where explicitly indicated.

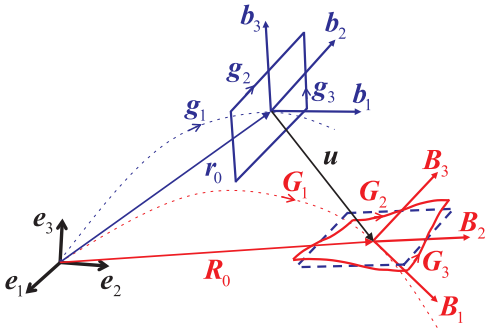

Fig. 1. Schematic of undeformed and deformed beam.

The material position vectors in the undeformed and deformed beam body can be expressed as

$$\boldsymbol{r} = \boldsymbol{r}_0 + x_\alpha \boldsymbol{b}_\alpha \tag{1}$$

$$\boldsymbol{R} = \boldsymbol{R}_0 + x_\alpha \boldsymbol{B}_\alpha + w_i(x_1,x_2,x_3)\boldsymbol{B}_i \tag{2}$$

with w_i representing the 3D unknown warping functions to describe the difference between the position of deformed body and those can be described by deformation of the reference curve x_1 in terms of $\boldsymbol{R}_0 + x_\alpha \boldsymbol{B}_\alpha$. $\boldsymbol{R}_0$ can also be expressed as

$$\boldsymbol{R}_0 = \boldsymbol{r}_0 + \boldsymbol{u} \tag{3}$$

where $\boldsymbol{u}$ denotes the beam displacement. Note $\boldsymbol{u}$ is not the displacement of some material point in the original structure. Rather it is the displacement field of the beam model (points on the beam reference line) we are constructing. In Eq. (2), we actually express $\boldsymbol{R}$ in terms of $\boldsymbol{R}_0$, $\boldsymbol{B}_i$, and w_i, which is six times redundant. Six constraints are needed to ensure a unique mapping. We can choose $\boldsymbol{B}_1$ to be tangent to the deformed reference line which introduces two constraints since we are building a model of Euler-Bernoulli type. As discussed in [16], we can also introduce the following four constraints for the warping functions:

$$\langle w_i \rangle = 0, \quad \langle w_{2,3} - w_{3,2} \rangle = 0 \tag{4}$$

From here and throughout the paper we assume a prismatic beam with uniform cross-sectional geometry. To derive a theory of the classical (Euler-Bernoulli) type, we define the following generalized 1D strains:

$$\boldsymbol{R}_0' = (1 + \gamma)\boldsymbol{B}_1 \tag{5}$$

$$\boldsymbol{B}_i' = \kappa_j \boldsymbol{B}_j \times \boldsymbol{B}_i \tag{6}$$

in which the upper prime denotes derivative to x_1, γ the axial strain, κ_1 the twist and κ_α the curvature of the deformed beam reference line. It is noted that these definitions of beam strains have nothing related with the well-known Euler-Bernoulli assumptions. Instead, we are constructing a model which is capable of capture extension (γ), torsion (κ_1), and bending in two directions (κ_α) with the possibility to capture all the 3D displacements, strains, and stresses due to these four fundamental deformation modes allowed in the Euler-Bernoulli beam model without apriori assuming that some components of the 3D fields vanish as most other theories do.

In Fig. 1, $\boldsymbol{g}_i$ denote the covariant base vectors of the undeformed body. And let the controvariant base vectors of the undeformed body denoted by $\boldsymbol{g}^i$. Then we have

$$\boldsymbol{g}^i = \boldsymbol{g}_i = \boldsymbol{b}_i \tag{7}$$

for prismatic beams. The covariant base vectors of the deformed configuration can be evaluated as

$$\boldsymbol{G}_k = \frac{\partial \boldsymbol{R}}{\partial x_k} \tag{8}$$

Together with Eq. (6), we have

$$\begin{aligned}\boldsymbol{G}_1 = {} & [1 + \gamma + w_1' - (x_2 + w_2)\kappa_3 + (x_3 + w_3)\kappa_2]\boldsymbol{B}_1 \\ & + [w_2' - (x_3 + w_3)\kappa_1 + w_1\kappa_3]\boldsymbol{B}_2 \\ & + [w_3' + (x_2 + w_2)\kappa_1 - w_1\kappa_2]\boldsymbol{B}_3\end{aligned} \tag{9}$$

$$\boldsymbol{G}_2 = w_{1,2}\boldsymbol{B}_1 + (1 + w_{2,2})\boldsymbol{B}_2 + w_{3,2}\boldsymbol{B}_3 \tag{10}$$

$$\boldsymbol{G}_3 = w_{1,3}\boldsymbol{B}_1 + w_{2,3}\boldsymbol{B}_2 + (1 + w_{3,3})\boldsymbol{B}_3 \tag{11}$$

Then the deformation gradient tensor can be formulated as the dyadic

product of $\boldsymbol{G}_i$ and $\boldsymbol{g}^i$ in the 3D Euclidean space, that is

$$\begin{aligned}\boldsymbol{F}&=\boldsymbol{G}_i\boldsymbol{g}^i=\boldsymbol{G}_1\boldsymbol{b}_1+\boldsymbol{G}_2\boldsymbol{b}_2+\boldsymbol{G}_3\boldsymbol{b}_3\\&=\begin{Bmatrix}\boldsymbol{B}_1\\\boldsymbol{B}_2\\\boldsymbol{B}_3\end{Bmatrix}^{\mathrm{T}}\begin{bmatrix}\underline{w_1'}+1+\gamma-(x_2+w_2)\kappa_3+(x_3+w_3)\kappa_2 & w_{1,2} & w_{1,3}\\ \underline{w_2'}+w_1\kappa_3-w_3\kappa_1-x_3\kappa_1 & 1+w_{2,2} & w_{2,3}\\ \underline{w_3'}-w_1\kappa_2+w_2\kappa_1+x_2\kappa_1 & w_{3,2} & 1+w_{3,3}\end{bmatrix}\begin{Bmatrix}\boldsymbol{b}_1\\\boldsymbol{b}_2\\\boldsymbol{b}_3\end{Bmatrix}\end{aligned} \tag{12}$$

which is a mix-based second-order tensor. The terms of $w_1\kappa_3$, $w_3\kappa_1$, $w_1\kappa_2$, and $w_2\kappa_1$ were neglected in the pioneering works on VABS [12–14,16] based on the assumption of small warping. However, warping is not necessarily small when the structure experiences material nonlinearity. Therefore, in this paper, these terms are retained regarding the finite warping.

Denote the beam cross-sectional characteristic dimension as h and the wavelength of deformation as l. Consequently, the intrinsic slender feature of beams can by described by $h/l \ll 1$. Using the bookkeeping parameter $\bar{\varepsilon}$ to express the magnitude of the maximum strain, we have

$$\bar{\varepsilon} = \max(\gamma, h\kappa_1, h\kappa_2, h\kappa_3) \tag{13}$$

Based on the previous works on VABS [12,14,16] it has been shown that

$$w_i = O(h\bar{\varepsilon}) \tag{14}$$

Because of the slenderness of beams, it is clear that the following is still true:

$$w_i' \sim \frac{w_i}{l} = O\left(\frac{h}{l}\bar{\varepsilon}\right) \ll \bar{\varepsilon} \tag{15}$$

In light of Eq. (15), the underlined w_i' terms in Eq. (9) can be neglected because their contributions to the governing functional are much smaller than the contributions of other terms. By neglecting these terms, the components of $\boldsymbol{F}$ in Eq. (12) can be arranged into a matrix as

$$\begin{aligned}F_{ij}&=\boldsymbol{B}_i\cdot(\boldsymbol{G}_k\boldsymbol{g}^k)\cdot\boldsymbol{b}_j\\&=\begin{bmatrix}1+\gamma-(x_2+w_2)\kappa_3+(x_3+w_3)\kappa_2 & w_{1,2} & w_{1,3}\\ w_1\kappa_3-w_3\kappa_1-x_3\kappa_1 & 1+w_{2,2} & w_{2,3}\\ w_1\kappa_2+w_2\kappa_1+x_2\kappa_1 & w_{3,2} & 1+w_{3,3}\end{bmatrix}\end{aligned} \tag{16}$$

Based on the concept of decomposition of rotation tensor [12], if the local rotation is small, which is the case for the framework of VABS except for the generalized solution for trapeze and Poynting effects [20,21], the 3D *Jaumann-Biot-Cauchy* strain components are given by

$$\Gamma_{ij} = \frac{1}{2}(F_{ij}+F_{ji})-\delta_{ij} \tag{17}$$

where δ_{ij} is the Kronecker delta. If the large local rotation is also considered for the kinematic nonlinearities, nonlinear strain definitions [22,23] should be applied.

According to [21], we can conclude that the warping function can be solved from the following variational statement:

$$\delta\mathscr{U} = \langle P_{ij}\delta\Gamma_{ij}\rangle = 0 \tag{18}$$

where P_{ij} are the components of the Cauchy stress tensor resolved into the beam cross-sectional triad. P_{ij} can be defined by

$$P_{ij} = \frac{\partial W}{\partial\Gamma_{ij}} \tag{19}$$

where W is the internal elastic energy in the deformed body.

2.2. Finite element implementation

The finite element method is used to solve the variational statement in Eq. (18). The 3D strain field in Eq. (17) can be expressed as

$$\Gamma = (\Gamma_h+\Gamma_\kappa)w + \Gamma_\epsilon\,\epsilon \tag{20}$$

with

$$\Gamma = [\Gamma_{11}\quad 2\Gamma_{12}\quad 2\Gamma_{13}\quad \Gamma_{22}\quad 2\Gamma_{23}\quad \Gamma_{33}]^{\mathrm{T}} \tag{21}$$

$$w = [w_1\quad w_2\quad w_3]^{\mathrm{T}} \tag{22}$$

$$\epsilon = [\epsilon_{(1)}\quad \epsilon_{(2)}\quad \epsilon_{(3)}\quad \epsilon_{(4)}]^{\mathrm{T}} = [\gamma\quad \kappa_1\quad \kappa_2\quad \kappa_3]^{\mathrm{T}} \tag{23}$$

The operators in Eq. (20) are defined as follows:

$$\Gamma_h = \begin{bmatrix}0&0&0\\ \frac{\partial}{\partial x_2}&0&0\\ \frac{\partial}{\partial x_3}&0&0\\ 0&\frac{\partial}{\partial x_2}&0\\ 0&\frac{\partial}{\partial x_3}&\frac{\partial}{\partial x_2}\\ 0&0&\frac{\partial}{\partial x_3}\end{bmatrix},\quad \Gamma_\epsilon = \begin{bmatrix}1&0&x_3&-x_2\\ 0&-x_3&0&0\\ 0&x_2&0&0\\ 0&0&0&0\\ 0&0&0&0\\ 0&0&0&0\end{bmatrix},\quad \Gamma_\kappa = \begin{bmatrix}0&-\kappa_3&\kappa_2\\ \kappa_3&0&-\kappa_1\\ -\kappa_2&\kappa_1&0\\ 0&0&0\\ 0&0&0\\ 0&0&0\end{bmatrix} \tag{24}$$

Let w be discretized using finite elements as

$$w = SV \tag{25}$$

Substituting Eq. (25) into Eq. (20) then into Eq. (18), we arrive at the following nonlinear system

$$\mathfrak{R}(V) = \langle[(\Gamma_h+\Gamma_\kappa)S]^{\mathrm{T}}P\rangle = 0 \tag{26}$$

where

$$P = [P_{11}\quad P_{12}\quad P_{13}\quad P_{22}\quad P_{23}\quad P_{33}]^{\mathrm{T}} \tag{27}$$

The Newton-Raphson method is applied to solve for V iteratively. Let V_o denote the initial guess, and let dV denote a correction to the V_o. In the neighborhood of V_o, $\mathfrak{R}$ in Eq. (26) can be expanded in a Taylor series with the high order terms neglected as

$$\mathfrak{R}(V_o+dV) \approx \mathfrak{R}(V_o) + \left(\frac{\partial\mathfrak{R}}{\partial V}\right)_{(V=V_o)} dV = 0 \tag{28}$$

which is iteratively solved for the correction dV to V_o by updating V_o as

$$V_o \leftarrow V_o + dV \tag{29}$$

until the updated value of V_o is converged during the iteration. In Eq. (28),

$$\frac{\partial\mathfrak{R}}{\partial V} = \langle[(\Gamma_h+\Gamma_\kappa)S]^{\mathrm{T}}[\mathbb{D}][(\Gamma_h+\Gamma_\kappa)S]\rangle \tag{30}$$

with $[\mathbb{D}]$ as the 6×6 matrix condensed from components of the tangent elasticity tensor

$$\mathbb{D}_{ijkl} = \frac{\partial P_{ij}}{\partial\Gamma_{kl}} = \beta_{im}\beta_{jn}\beta_{kp}\beta_{lq}\mathbb{L}_{mnpq} \tag{31}$$

where $\mathbb{L}_{mnpq}$ is the tangent elasticity tensor in $\boldsymbol{t}_i$ lamina bases, and β_{ij} is the component of the direction cosine matrix of transformation from $\boldsymbol{t}_i$ to $\boldsymbol{b}_i$ following the coordinate convention shown in Fig. 2. Under the same convention, the stress and strain tensors can be transformed by

$$P_{ij} = \beta_{ik}\beta_{jl}\sigma_{kl},\quad \Gamma_{ij} = \beta_{ik}\beta_{jl}\varepsilon_{kl} \tag{32}$$

where σ_{kl} and ε_{kl} are stress and strain components resolved in the material coordinates $\boldsymbol{t}_i$ of each lamina.

Meanwhile, the four constraints in Eq. (4) can be written in a matrix form as

$$\langle(F_c S)\rangle V = 0 \tag{33}$$

with

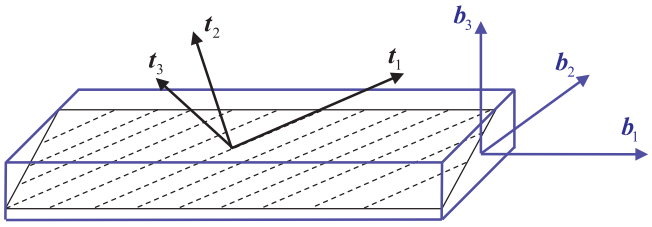

Fig. 2. VABS coordinate convention.

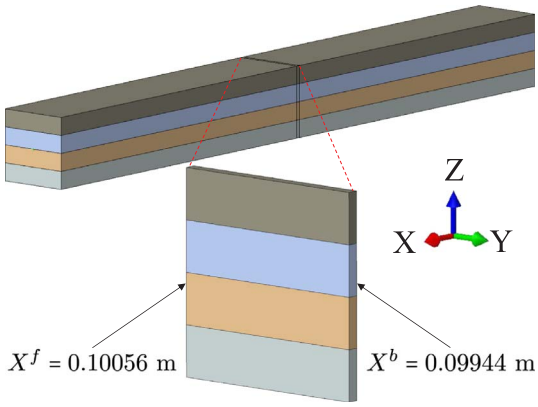

Fig. 3. Partition of the 3D $[45/-45]_s$ square-section composite beam.

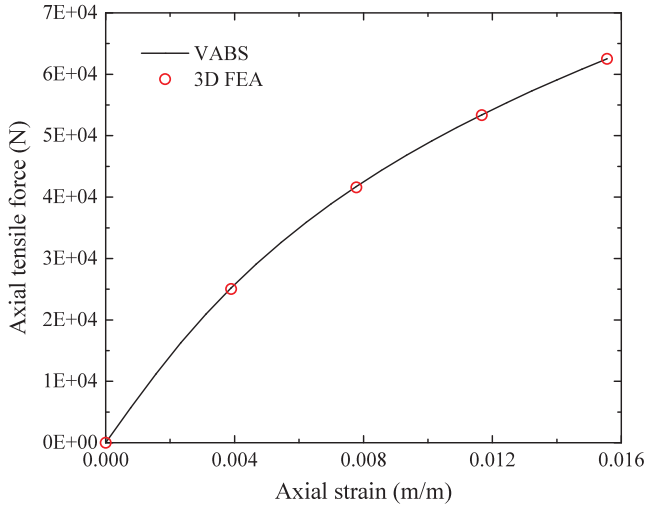

Fig. 4. Comparison of extensional constitutive data.

$$F_c = \begin{bmatrix} 1 & 0 & 0 \\ 0 & 1 & 0 \\ 0 & 0 & 1 \\ 0 & \frac{\partial}{\partial x_3} & -\frac{\partial}{\partial x_2} \end{bmatrix} \tag{34}$$

Giving the beam strain ϵ in the form of stepwise updating of ϵ_o by an increment $d\epsilon$ as

$$\epsilon = \epsilon_o + d\epsilon \tag{35}$$

we can solve for dV iteratively for each loading step using

$$\Xi \begin{Bmatrix} dV \\ [\lambda]_{4\times 1} \end{Bmatrix} = -\begin{Bmatrix} \langle [(\Gamma_h + \Gamma_\kappa)S]^T P \rangle \\ [0]_{4\times 1} \end{Bmatrix} \tag{36}$$

with

$$\Xi = \begin{bmatrix} \langle [(\Gamma_h + \Gamma_\kappa)S]^T [\mathbb{D}] [(\Gamma_h + \Gamma_\kappa)S] \rangle & \langle (F_c S)^T \rangle \\ \langle (F_c S) \rangle & [0]_{4\times 4} \end{bmatrix}$$

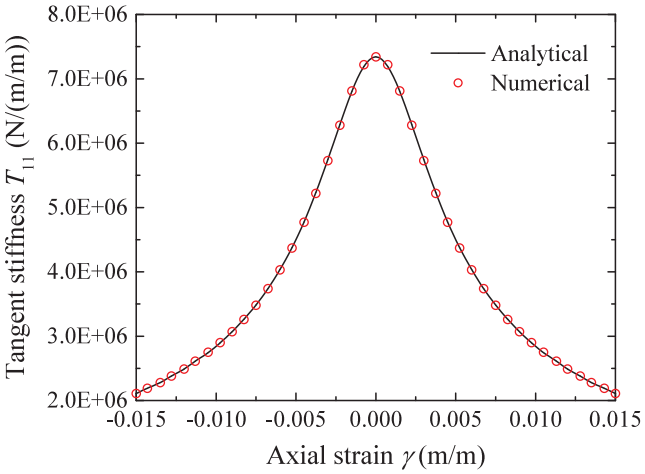

Fig. 5. Tangent beam stiffness predicted by VABS as a function of axial strain.

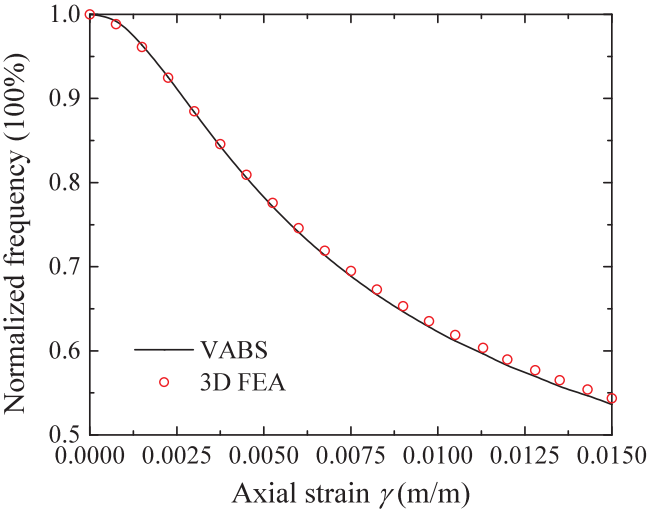

Fig. 6. Reduction of the natural frequency due to pre-strain and shear nonlinearity.

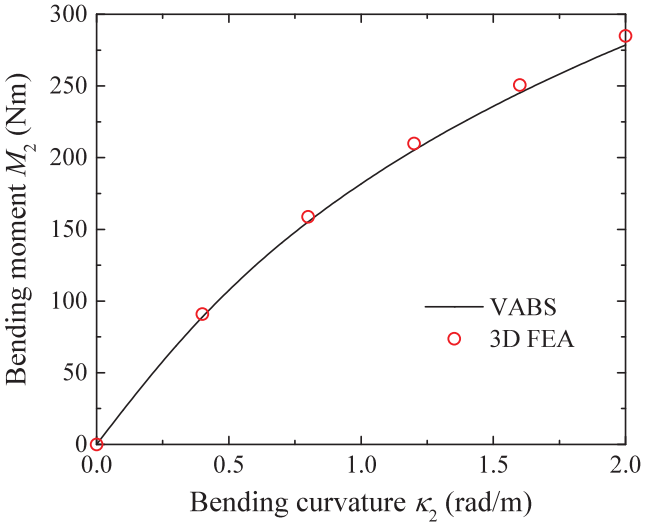

Fig. 7. Comparison of bending constitutive data.

and $[\lambda]_{4\times 1}$ as a column matrix consisting of Lagrange multipliers.

To calculate the sectional stress resultants, define the following column matrix

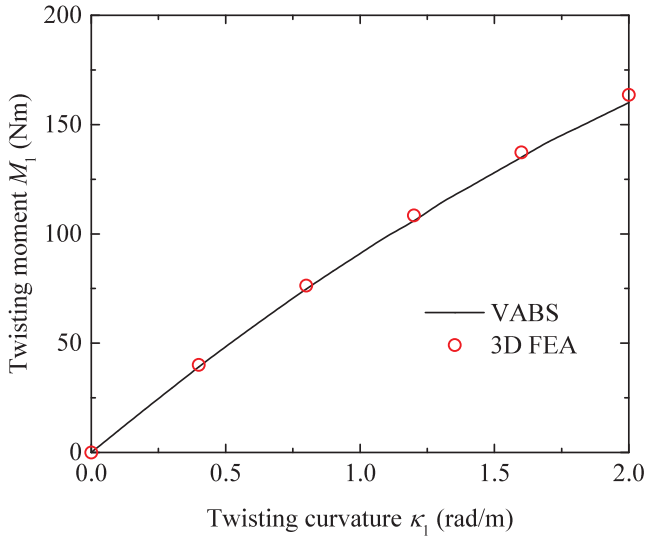

Fig. 8. Comparison of twisting constitutive data.

$$\bar{\delta}_{(i)} = \frac{\partial \epsilon}{\partial \epsilon_{(i)}}[\delta_{i1} \quad \delta_{i2} \quad \delta_{i3} \quad \delta_{i4}]^{\mathrm{T}}, \qquad i = 1,2,3,4 \tag{37}$$

where $\delta_{(ij)} = 1$ if $i = j$ and $\delta_{(ij)} = 0$ if $i \neq j$, in which $i, j = 1, 2, 3, 4$. In addition, denote

$$R = [R_{(1)} \quad R_{(2)} \quad R_{(3)} \quad R_{(4)}]^{\mathrm{T}} = [F_1 \quad M_1 \quad M_2 \quad M_3]^{\mathrm{T}} \tag{38}$$

According to [2], it is known that the elastic strain energy W can be obtained by

$$W = \Gamma^{\mathrm{T}} P - W^* \tag{39}$$

where W^* denotes the complimentary energy. Regarding the definition of strain

$$\Gamma = \frac{\partial W^*}{\partial P} \tag{40}$$

we can evaluate the sectional resultant components in R corresponding to the strains ϵ as

$$R_{(i)} = \frac{\partial \langle W \rangle}{\partial \epsilon_{(i)}} = \left\langle \Gamma^{\mathrm{T}} \frac{\partial P}{\partial \Gamma} \frac{\partial \Gamma}{\partial \epsilon_{(i)}} + \left[\frac{\partial \Gamma}{\partial \epsilon_{(i)}}\right]^{\mathrm{T}} P - \left(\frac{\partial W^*}{\partial P}\right)^{\mathrm{T}} \frac{\partial P}{\partial \Gamma} \frac{\partial \Gamma}{\partial \epsilon_{(i)}} \right\rangle = \left\langle \left[\frac{\partial \Gamma}{\partial \epsilon_{(i)}}\right]^{\mathrm{T}} P \right\rangle, \quad i = 1,2,3,4 \tag{41}$$

where

$$\frac{\partial \Gamma}{\partial \epsilon_{(i)}} = \Gamma_\epsilon \bar{\delta}_{(i)} + \frac{\partial (\Gamma_\kappa S)}{\partial \epsilon_{(i)}} V + (\Gamma_h + \Gamma_\kappa) S \frac{\partial V}{\partial \epsilon_{(i)}} \tag{42}$$

It is possible to prove that the derivatives of the warping values on the beam strains do not affect the resultant R. Due to the discretization, nodal warping values are variables independent of the sectional coordinates, then V, dV, and $\frac{\partial V}{\partial \epsilon_i}$ can be extracted out of the sectional integration. In light of Eq. (26),

$$\left\langle \left[(\Gamma_h + \Gamma_\kappa) S \frac{\partial V}{\partial \epsilon_{(j)}}\right]^{\mathrm{T}} P \right\rangle = \left[\frac{\partial V}{\partial \epsilon_{(j)}}\right]^{\mathrm{T}} \langle [(\Gamma_h + \Gamma_\kappa) S]^{\mathrm{T}} P \rangle = \left[\frac{\partial V}{\partial \epsilon_{(j)}}\right]^{\mathrm{T}} \mathfrak{R} = 0 \tag{43}$$

As a result,

$$R_{(i)} = \left\langle \left[\Gamma_\epsilon \bar{\delta}_{(i)} + \frac{\partial (\Gamma_\kappa S)}{\partial \epsilon_{(i)}} V\right]^{\mathrm{T}} P \right\rangle, \quad i = 1,2,3,4 \tag{44}$$

In addition, the tangent beam cross-sectional stiffness can be expressed as

$$T_{ij} = \frac{\partial R_{(i)}}{\partial \epsilon_{(j)}} = \left\langle \left[\frac{\partial (\Gamma_\kappa S)}{\partial \epsilon_{(i)}} \frac{\partial V}{\partial \epsilon_{(j)}}\right]^{\mathrm{T}} P \right\rangle + \left\langle \left[\Gamma_\epsilon \bar{\delta}_{(i)} + \frac{\partial (\Gamma_\kappa S)}{\partial \epsilon_{(i)}} V\right]^{\mathrm{T}} [\mathbb{D}] \left[\frac{\partial \Gamma}{\partial \epsilon_{(i)}}\right] \right\rangle, \quad i, j = 1,2,3,4 \tag{45}$$

Derivatives of warping values with respect to the beam strain $\frac{\partial V}{\partial \epsilon_{(i)}}$ can be computed using Eq. (26). Taking derivatives with respect to $\epsilon_{(i)}$ on both sides gives

$$\frac{\partial \mathfrak{R}}{\partial \epsilon_{(i)}} = \left\langle \left[\frac{\partial (\Gamma_\kappa S)}{\partial \epsilon_{(i)}}\right]^{\mathrm{T}} P \right\rangle + \left\langle [(\Gamma_h + \Gamma_\kappa) S]^{\mathrm{T}} [\mathbb{D}] \left[\frac{\partial \Gamma}{\partial \epsilon_{(i)}}\right] \right\rangle = 0, \quad i = 1,2,3,4 \tag{46}$$

In light of the warping constraints Eq. (33), we have the same constraints on $\frac{\partial V}{\partial \epsilon_{(i)}}$ as

$$\langle (F_c S) \rangle \frac{\partial V}{\partial \epsilon_{(i)}} = 0 \tag{47}$$

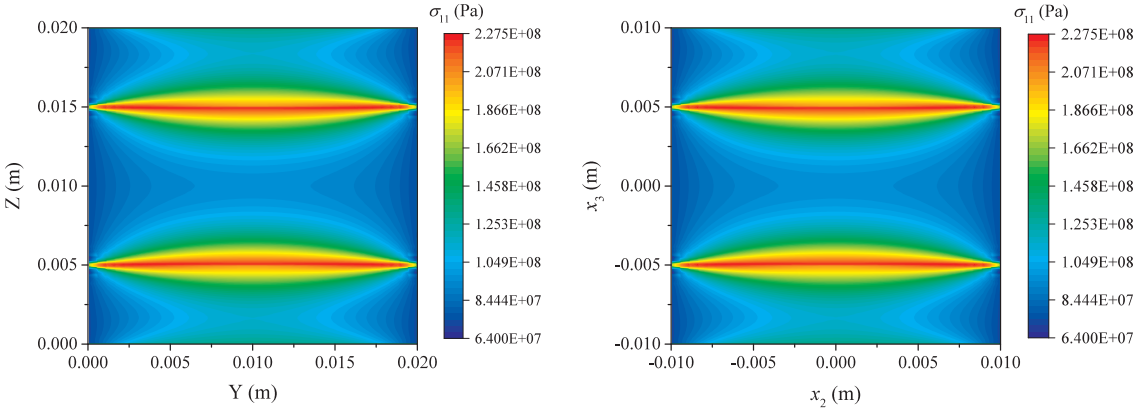

(a) 3D FEA. (b) VABS.

Fig. 9. Comparison of stress σ_{11} contour plots at $\gamma = 0.01556$.

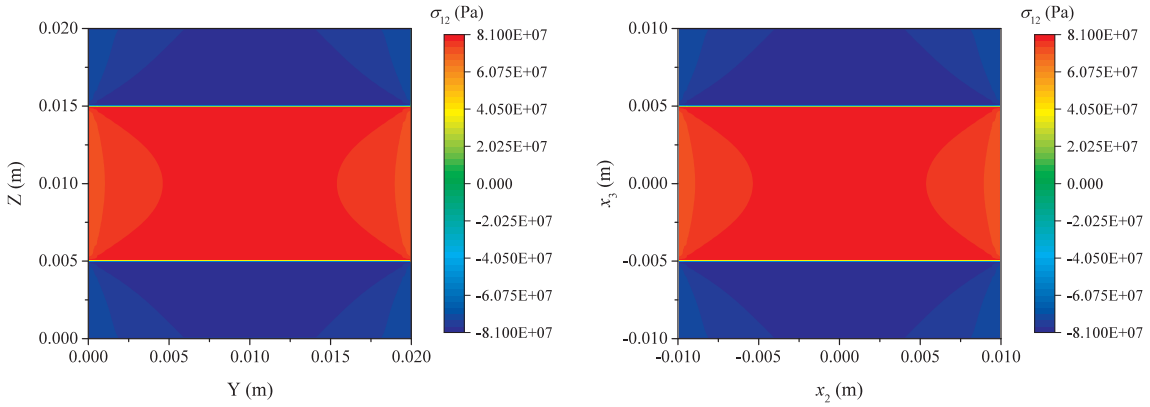

Fig. 10. Comparison of stress σ_{12} contour plots at $\gamma = 0.01556$.

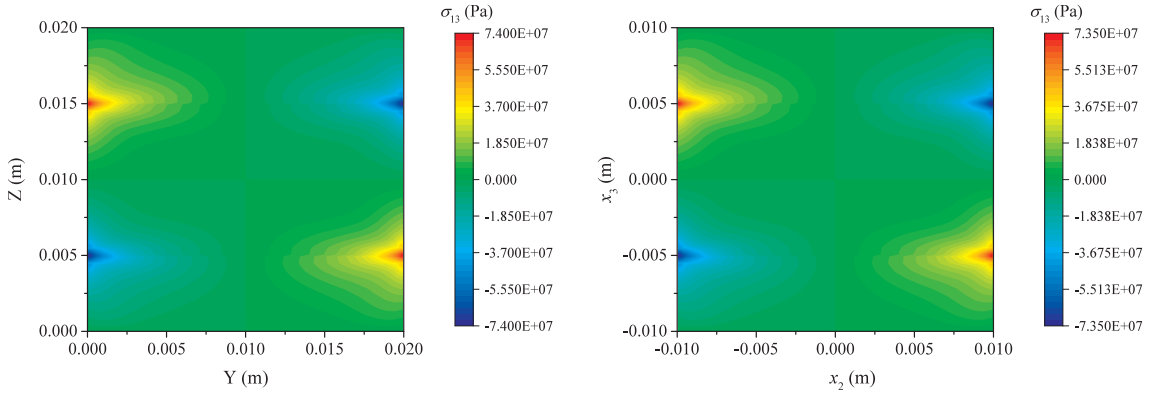

Fig. 11. Comparison of stress σ_{13} contour plots at $\gamma = 0.01556$.

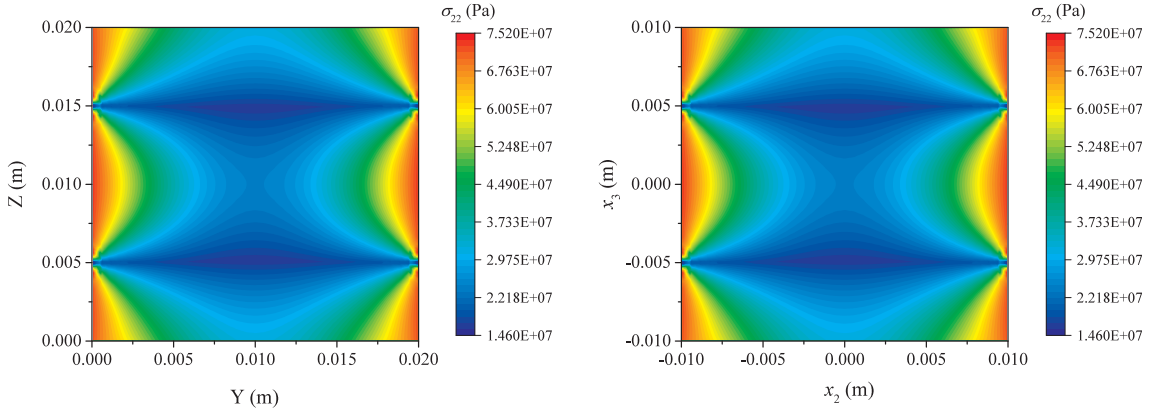

Fig. 12. Comparison of stress σ_{22} contour plots at $\gamma = 0.01556$.

Combining Eqs. (46) and (47), $\frac{\partial V}{\partial \epsilon_{(i)}}$ can be solved by

$$\Xi \begin{Bmatrix} \frac{\partial V}{\partial \epsilon_{(i)}} \\ [\lambda]_{4\times 1} \end{Bmatrix} = -\begin{Bmatrix} \left\langle \left[\frac{\partial(\Gamma_\kappa S)}{\partial \epsilon_{(i)}}\right]^{\mathrm{T}} P + [(\Gamma_h + \Gamma_\kappa)S]^{\mathrm{T}}[\mathbb{D}]\left[\Gamma_\epsilon \bar{\delta}_{(i)} + \frac{\partial(\Gamma_\kappa S)}{\partial \epsilon_{(j)}} V\right] \right\rangle \\ [0]_{4\times 1} \end{Bmatrix}, \quad i = 1,2,3,4 \tag{48}$$

3. Numerical examples

3.1. Nonlinear beam constitutive law

To validate the present VABS theory, consider the third-order elastic nonlinear shear model proposed by Hahn and Tsai [2], that is,

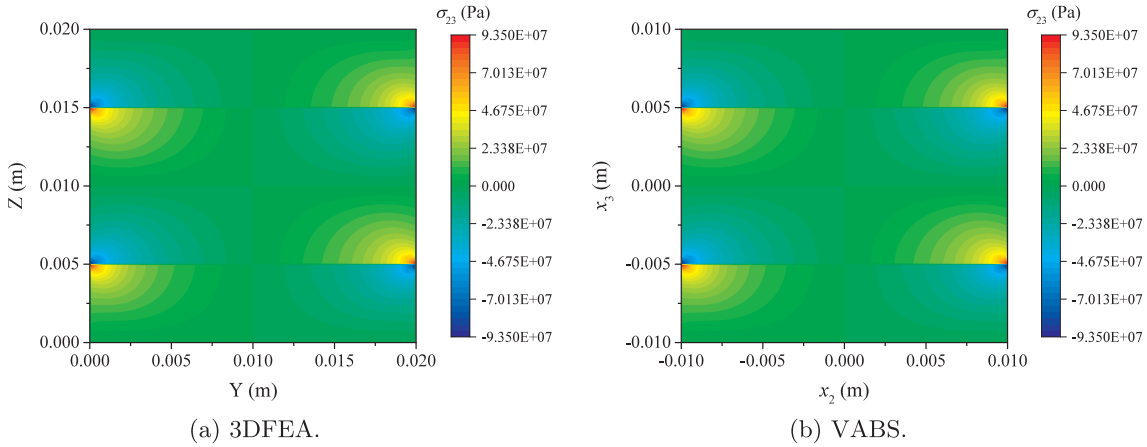

Fig. 13. Comparison of stress σ_{23} contour plots at $\gamma = 0.01556$.

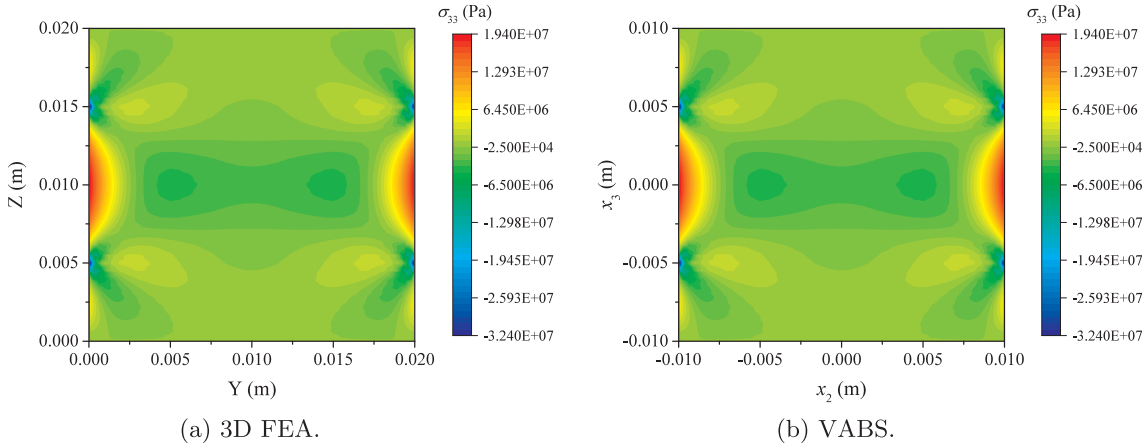

Fig. 14. Comparison of stress σ_{33} contour plots at $\gamma = 0.01556$.

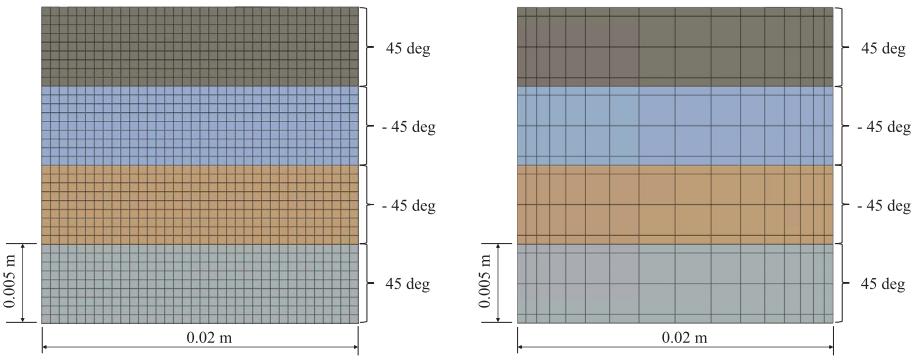

Fig. 15. Examples of the meshing scheme.

Table 1
Comparison of computation aspects.

Computation aspect	3D FEA	Nonlinear VABS
Time	19 h 39 min 41 s	3 min 43 s
Increments	4	20
Multi-Processor	40	1
Multi-GPU	4	0

$$2\varepsilon_{12} = \frac{\sigma_{12}}{G_{12}} + \frac{\sigma_{12}^3}{X_{12}} \tag{49}$$

So the tangent compliance matrix can be obtained by

$$[\mathbb{S}] = [\mathbb{H}] + 3\frac{\sigma_{12}^2}{X_{12}}[\mathbb{Q}] \tag{50}$$

where

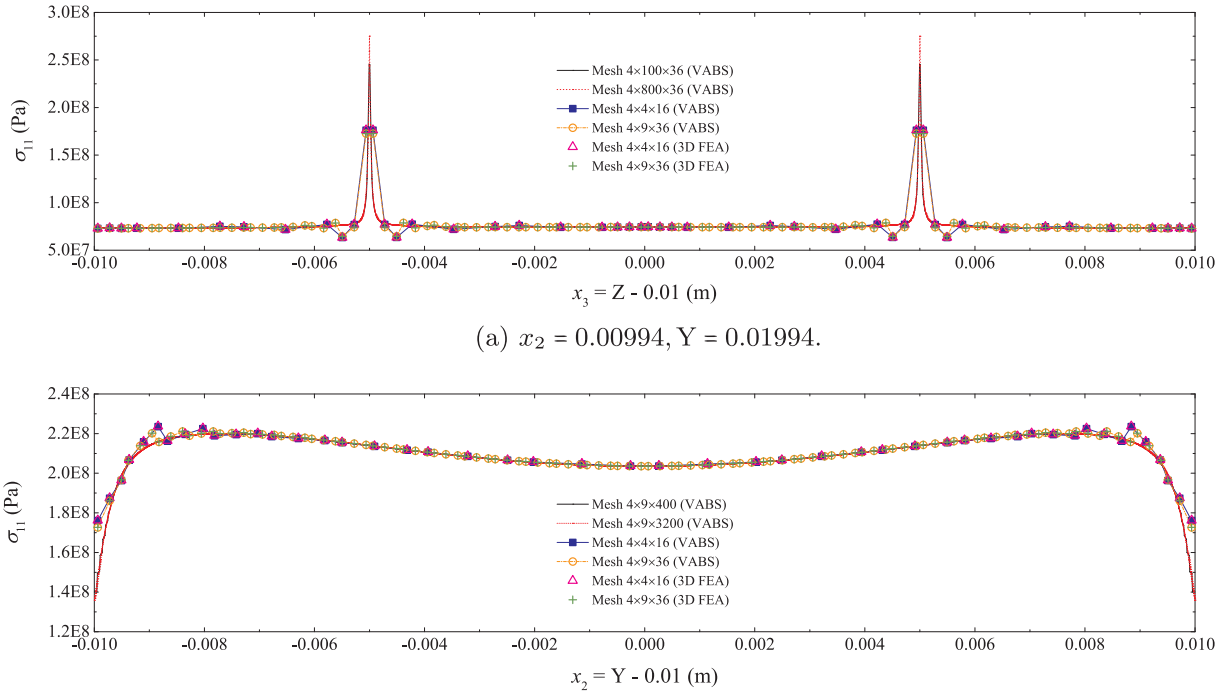

Fig. 16. Comparison of stress σ_{11} curve plots at $\gamma = 0.01556$.

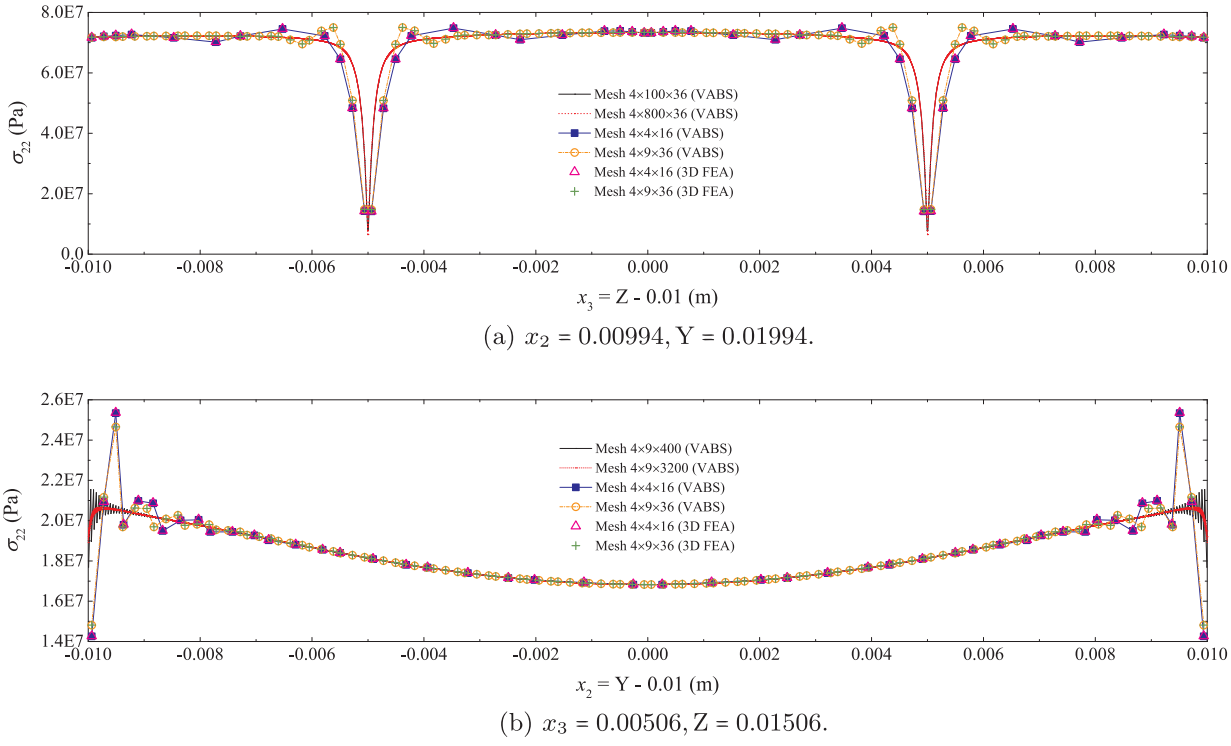

Fig. 17. Comparison of stress σ_{22} curve plots at $\gamma = 0.01556$.

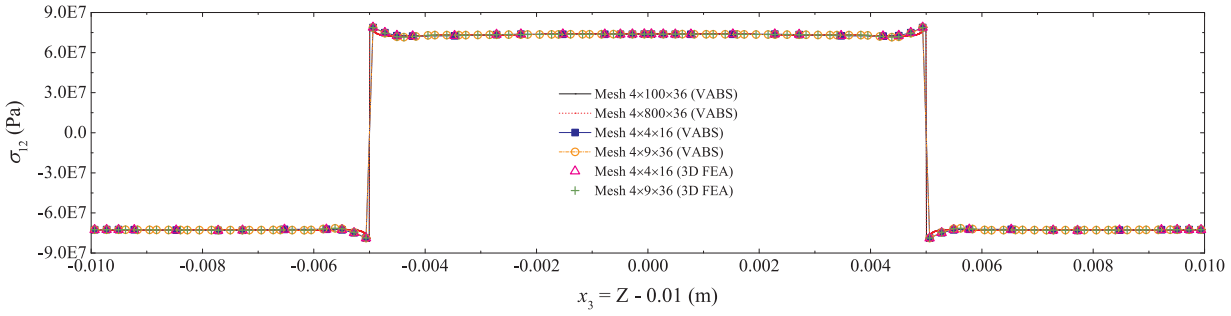

(a) $x_2 = 0.00994, \mathrm{Y} = 0.01994.$

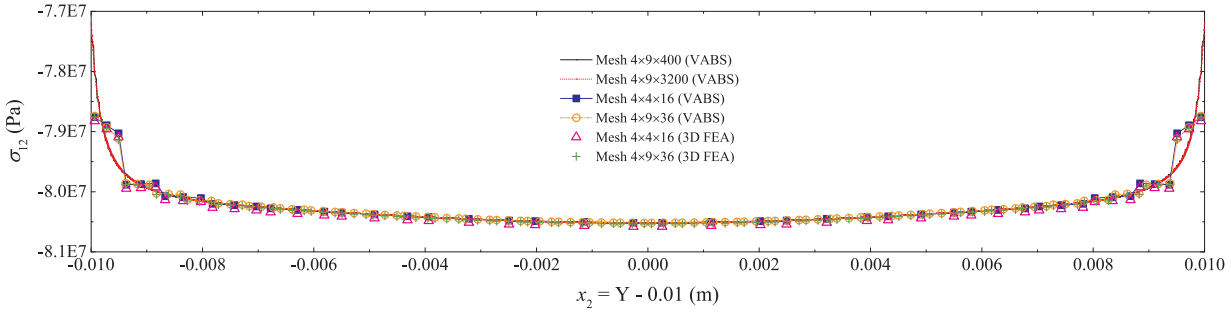

(b) $x_3 = 0.00506, \mathrm{Z} = 0.01506.$

Fig. 18. Comparison of stress σ_{12} curve plots at $\gamma = 0.01556$.

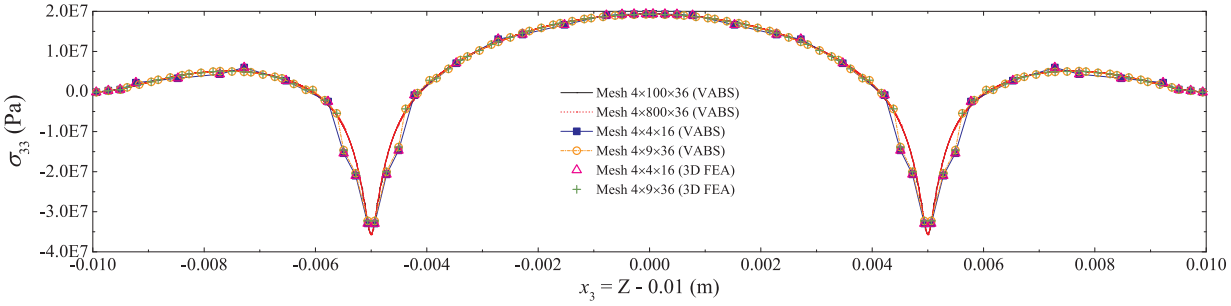

(a) $x_2 = 0.00994, \mathrm{Y} = 0.01994.$

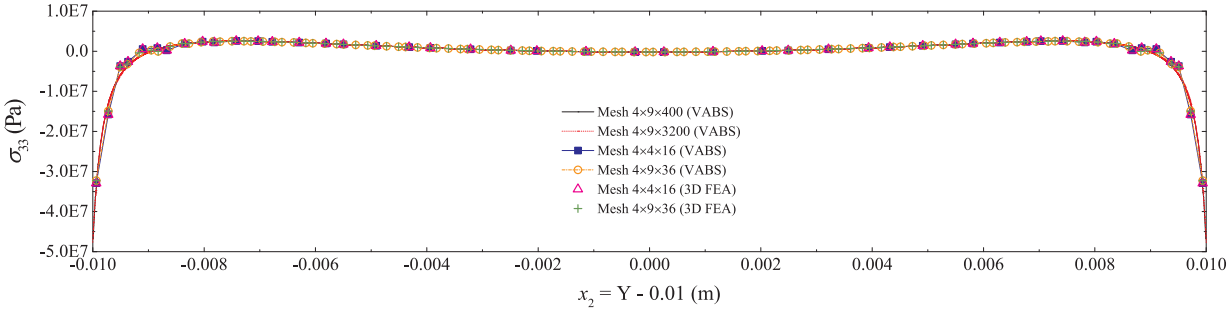

(b) $x_3 = 0.00506, \mathrm{Z} = 0.01506.$

Fig. 19. Comparison of stress σ_{33} curve plots at $\gamma = 0.01556$.

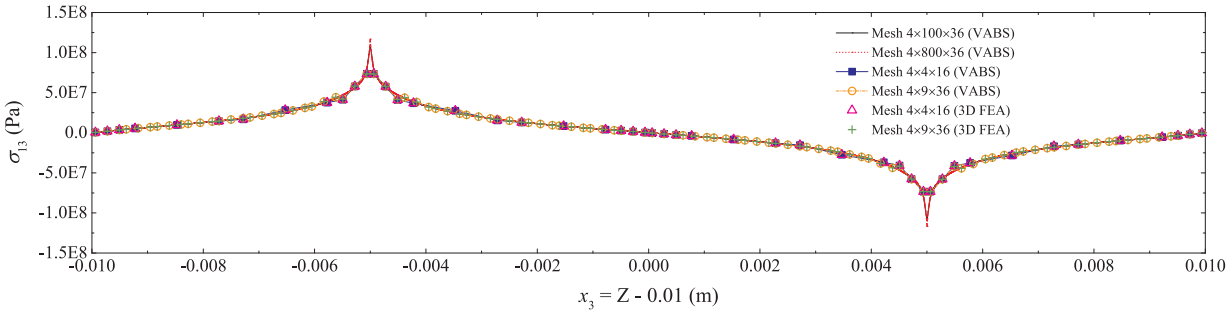

(a) $x_2 = 0.00994, \mathrm{Y} = 0.01994.$

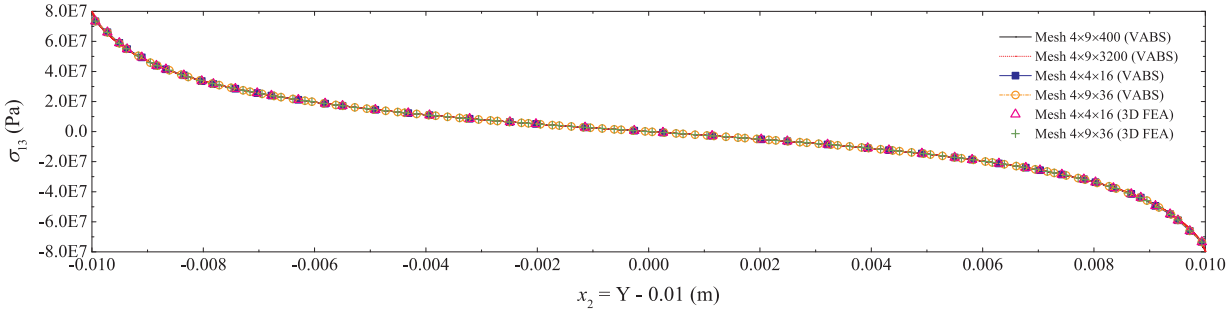

(b) $x_3 = 0.00506, \mathrm{Z} = 0.01506.$

Fig. 20. Comparison of stress σ_{13} curve plots at $\gamma = 0.01556$.

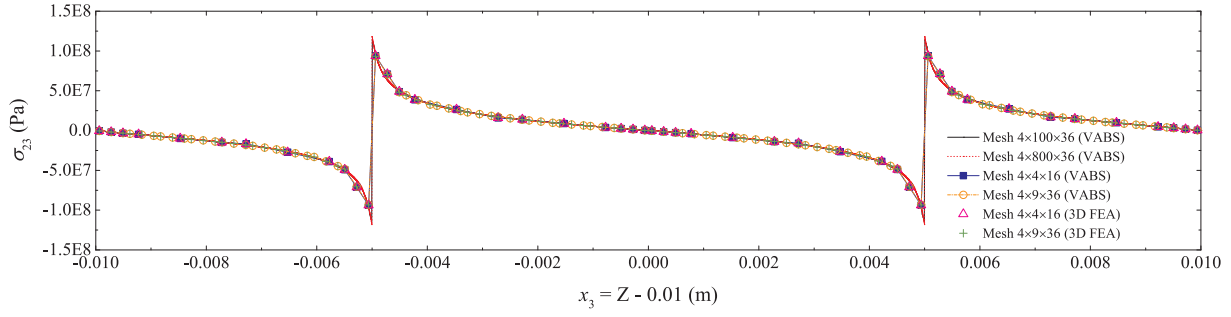

(a) $x_2 = 0.00994, \mathrm{Y} = 0.01994.$

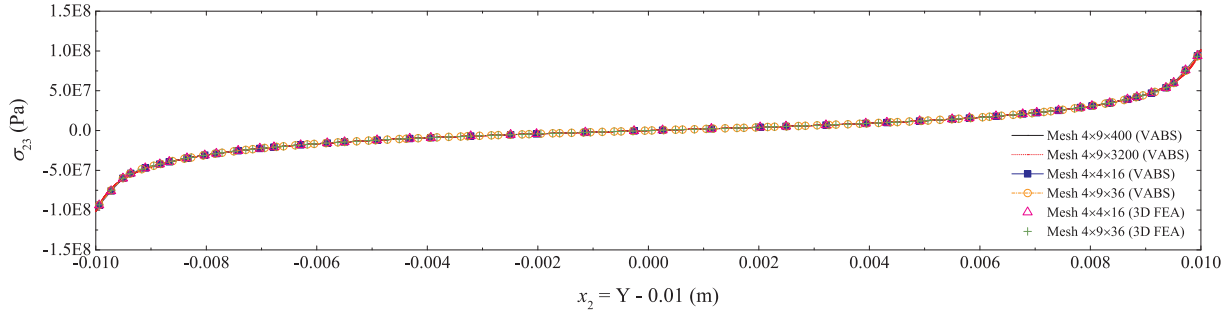

(b) $x_3 = 0.00506, \mathrm{Z} = 0.01506.$

Fig. 21. Comparison of stress σ_{23} curve plots at $\gamma = 0.01556$.

Table 2
Mesh dependency of global beam behaviors.

Meshing scheme	F_1 (N) $\gamma = 0.01556$	M_1 (Nm) $\kappa_1 = 2.0$ rad/m	M_2 (Nm) $\kappa_2 = 2.0$ rad/m
4 × 4 × 16 (3D FEA)	62559.20	163.62	285.13
4 × 9 × 36 (3D FEA)	62523.07	163.61	284.98
4 × 4 × 16 (VABS)	62509.54	160.48	278.51
4 × 9 × 36 (VABS)	62508.15	160.47	278.50
4 × 100 × 36 (VABS)	62506.11	160.47	278.49
4 × 9 × 400 (VABS)	62507.02	160.47	278.50
4 × 800 × 36 (VABS)	62506.07	160.47	278.49
4 × 9 × 3200 (VABS)	62507.00	160.47	278.50

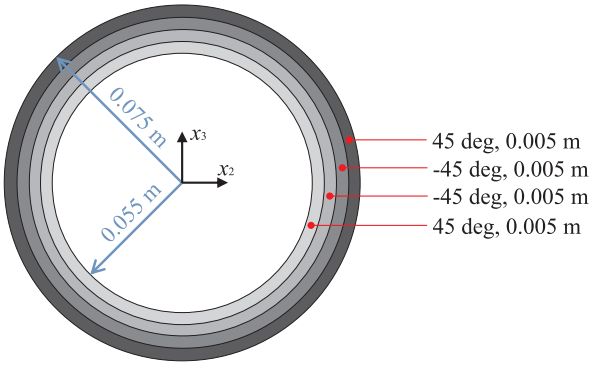

Fig. 22. Cross-sectional geometry and layout of the tube section.

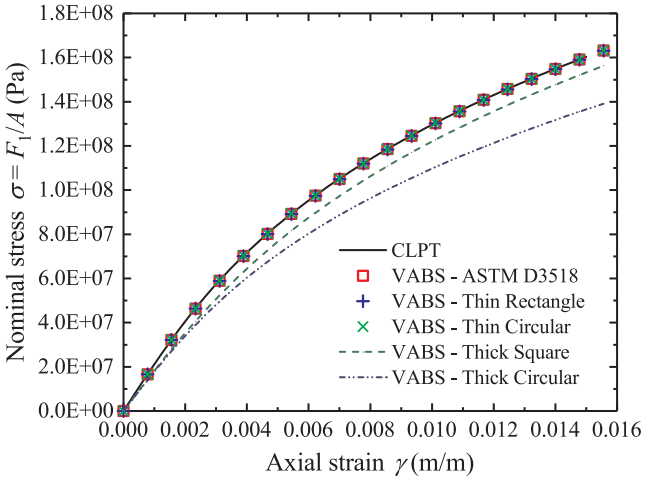

Fig. 23. Comparison of performances of virtual beam coupons.

$$[\mathbb{H}] = \begin{bmatrix} \frac{1}{E_1} & 0 & 0 & -\frac{\nu_{21}}{E_2} & 0 & -\frac{\nu_{31}}{E_3} \\ 0 & \frac{1}{G_{12}} & 0 & 0 & 0 & 0 \\ 0 & 0 & \frac{1}{G_{13}} & 0 & 0 & 0 \\ -\frac{\nu_{12}}{E_1} & 0 & 0 & \frac{1}{E_2} & 0 & -\frac{\nu_{32}}{E_3} \\ 0 & 0 & 0 & 0 & \frac{1}{G_{23}} & 0 \\ -\frac{\nu_{13}}{E_1} & 0 & 0 & -\frac{\nu_{23}}{E_2} & 0 & \frac{1}{E_3} \end{bmatrix}, \quad [\mathbb{Q}] = \begin{bmatrix} 0 & 0 & 0 & 0 & 0 & 0 \\ 0 & 1 & 0 & 0 & 0 & 0 \\ 0 & 0 & 0 & 0 & 0 & 0 \\ 0 & 0 & 0 & 0 & 0 & 0 \\ 0 & 0 & 0 & 0 & 0 & 0 \\ 0 & 0 & 0 & 0 & 0 & 0 \end{bmatrix} \tag{51}$$

The elastic properties are $E_1 = 155.65$ GPa, $E_2 = E_3 = 8.977$ GPa, $\nu_{12} = \nu_{13} = 0.3197, \nu_{23} = 0.44, G_{13} = 4.88$ GPa, $G_{23} = 3.117$ GPa, $G_{12} = 6.18345$ GPa, and $X_{12} = 3.3984 \times 10^{25}$ Pa^3. The X_{12} value is obtained by fitting the shear stress-strain measured from the tensile tests of $[45/-45]_{4s}$ coupon composed by IM7/977-3 graphite/epoxy lamina [24]. According to Hahn and Tsai [2], the X_{12} value is reported to be 13.8764×10^{25} Pa^3 for Morganite II/4617 system.

The geometry and mesh of the cross section of a $[45/-45]_s$ square-sectioned laminate beam is analyzed by VABS. The layer thickness is 0.005 m, and the square-sectional edge is 0.02 m. Each layer contains 9 evenly spaced mesh divisions in the through-thickness dimension and 36 evenly spaced mesh divisions in the transverse dimension. The section is meshed with 1296 eight-node quadrilateral elements, containing 4033 nodes. The geometry, layout, and mesh of the cross section can be found in Fig. 15(a). The corresponding 3D model is analyzed by using the commercial FEA software Abaqus [25]. The material is applied by programming user-defined material subroutine (UMAT). The length of the beam is 0.2 m, ten times its cross-sectional width. All nodes on one of the beam end section are totally fixed. The nodes on the other end section are completely kinematically constrained to a reference point located at the geometric center of the section. The displacement boundary condition is applied at this reference point with $U_x = 0.015 \times 0.2$ m. The reaction force is measured from the reference point. The 3D laminate body is analyzed using a global-local approach by partitioning the structure into three parts including one small part in the middle and two large parts on the sides, as shown in Fig. 3. The three parts have the same mesh schema in Y-Z plane as the cross-sectional mesh analyzed by VABS shown in Fig. 15(a). In Z direction, the large parts are each meshed with 179 divisions, and the small part is meshed with 4 divisions. The large parts are each meshed by 231,987 20-node C3D20 elements containing 970,991 nodes. The small part is meshed by 5184 20-node brick elements (C3D20) containing 25,641 nodes, where the nodal coordinates and displacements are reported from the two cross sections located at $X^f = 0.10056$ m and $X^b = 0.09944$ m, respectively.

To validate the VABS predictions, it is necessary to make sure the axial strains applied on the 3D FEA model and VABS sectional model are the same. The axial strain input into VABS is computed from the 3D FEA model. The averaged final axial displacements from these two sets of nodes at $X^f = 0.10056$ m and $X^b = 0.09944$ m are $U_x^f = 0.0015087$ m and $U_x^b = 0.0014914$ m, respectively. Consequently, the final axial strain of the effective 1D beam can be computed as

$$\gamma = \frac{U_x^f - U_x^b}{X^f - X^b} = 0.01556 \tag{52}$$

This strain is input into VABS to obtain the nonlinear beam sectional effective force-strain constitutive curve. This curve is compared with the reaction force-strain data reported from the Abaqus 3D FEA in Fig. 4, from where good comparison is observed.

A good fitting equation to the VABS numerical prediction of the axial beam constitutive law shown in Fig. 4 could be

$$\gamma = c_1 F_1 + c_2 F_1^3 \tag{53}$$

where the fitted constants are $c_1 = 1.36238 \times 10^{-7}$ (m/m)/N and $c_2 = 2.88674 \times 10^{-17}$ (m/m)^3/N^3. Solving Eq. (53) for F_1 results in

$$F_1 = \frac{s_1 + s_2 (s_3\gamma + s_4\sqrt{s_5 + s_6\gamma^2})^{2/3}}{(s_3\gamma + s_4\sqrt{s_5 + s_6\gamma^2})^{1/3}} \tag{54}$$

where the constants are

$$s_1 = -\left(\frac{2}{3}\right)^{\frac{1}{3}} c_1, \quad s_2 = \left(2^{\frac{1}{3}} 3^{\frac{2}{3}} c_2\right)^{-1}, \quad s_3 = 9c_2^2, \quad s_4 = \sqrt{2}, \quad s_5 = 4c_1^3 c_2^3, \quad s_6 = 27c_2^4 \tag{55}$$

From Eq. (54) the beam tangent stiffness can be computed as

$$T_{11} = \frac{\partial F_1}{\partial \gamma} = \frac{(s_4 s_6 \gamma + s_3\sqrt{s_5 + s_6\gamma^2})[-s_1 + s_2(s_3\gamma + s_4\sqrt{s_5 + s_6\gamma^2})^{2/3}]}{3\sqrt{s_5 + s_6\gamma^2}(s_3\gamma + s_4\sqrt{s_5 + s_6\gamma^2})^{1/3}} \tag{56}$$

This analytical expression agrees the numerical results of T_{11} predicted by VABS, as shown in Fig. 5.

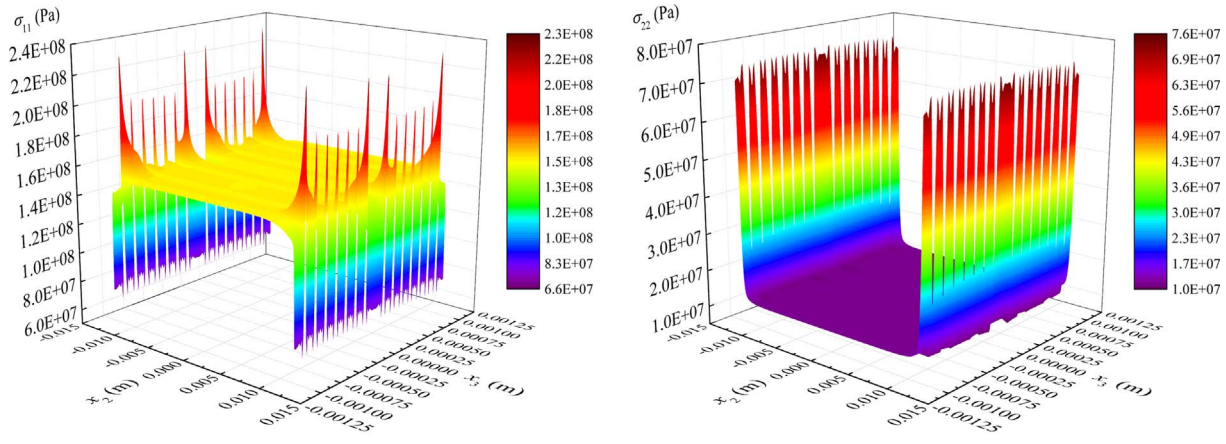

(a) σ_{11}.

(b) σ_{22}.

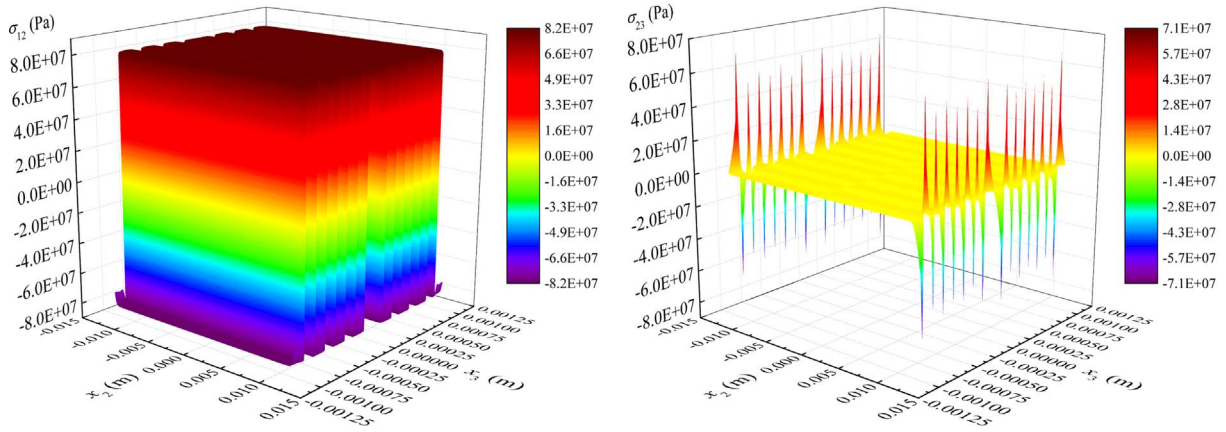

(c) σ_{12}.

(d) σ_{23}.

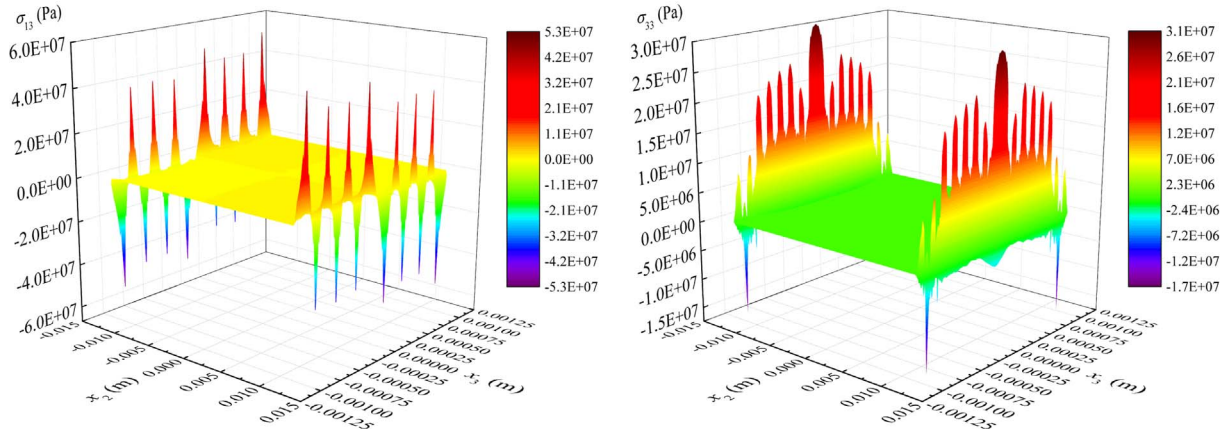

(e) σ_{13}.

(f) σ_{33}.

Fig. 24. Local stress fields on the cross-sectional domain of ASTM D3518 virtual coupon at $\gamma = 0.01556$.

To validate the T_{11} from VABS with the result of 3D FEA, we examine the extension mode natural frequency ω of the beam under the axial pre-strain. Under the circumstance of pinned-pinned boundary conditions, ω can be computed by

$$\omega = \frac{\pi}{l}\sqrt{\frac{T_{11}}{\rho_A}} \tag{57}$$

where l is the beam length. The natural frequencies under various axial pre-strains are normalized by the natural frequency without any pre-strain. These normalized values are plotted in Fig. 6 with respect to the corresponding pre-strains. It can be seen that the natural frequency is reduced by the introduction of the pre-strain and the nonlinearity.

To examine the bending behavior, in the 3D FE model with brick elements, the nodes on the two end sections of the beam are both kinematically constrained to the reference points located at the geometric centers of the two sections, respectively. The first reference point at $x = 0$ is fixed in U_x and U_z and is applied with a rotation $-\theta_y$ (θ_2 in VABS coordinate convention). The second reference point at $x = l$ (l is the

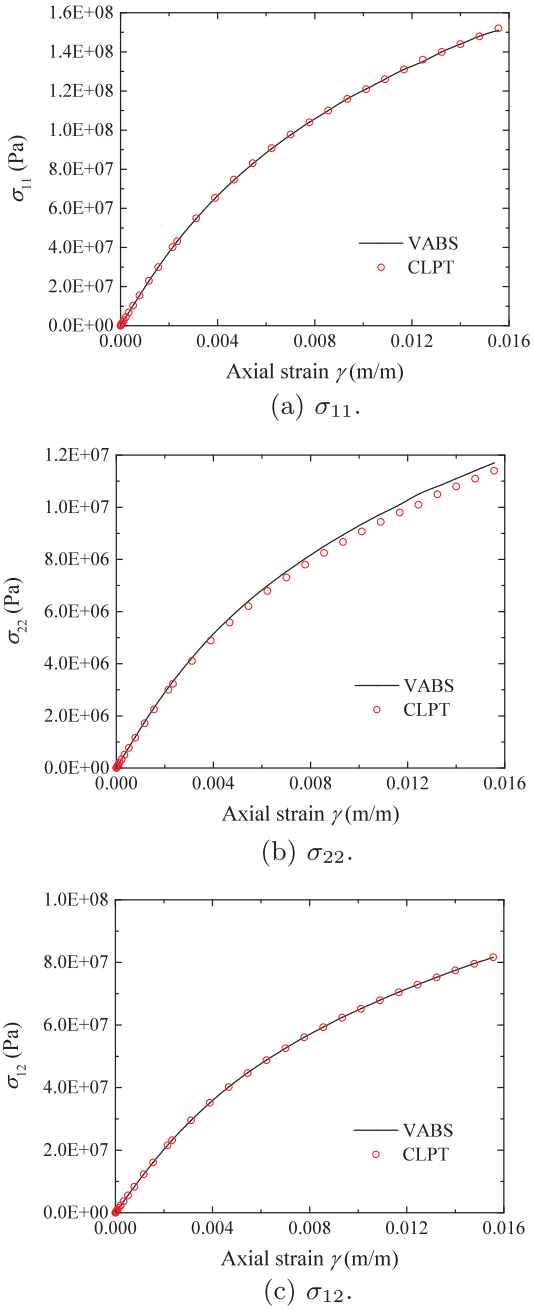

Fig. 25. Comparison of the in-plane stresses of ASTM D3518 virtual coupon predicted by VABS and CLPT. (The values of VABS are obtained by averaging the values at the integration points located at $x_2 = \pm 4.63\text{E}-6$.)

overall beam length) is fixed only in U_z and is applied with a rotation θ_y. These boundary conditions and constraints approximate a uniformly distributed bending curvature κ_y (κ_2 in VABS coordinate convention). The reaction bending moment M_y (M_2 in VABS coordinate convention) on the second reference point is requested from the solution data base. The bending curvature of the 3D beam is approximately estimated by

$$\kappa_y = 2\frac{\theta_y}{l} \tag{58}$$

This bending curvature is input into VABS to obtain the nonlinear beam bending constitutive curve. This curve is compared with the reaction bending moment and curvature data reported from the 3D FEA, as shown in Fig. 7.

In studying the twisting behavior of the beam, the layup is switched to $[0/90]_s$ while the geometry and the mesh are kept unchanged. In the 3D FEA, the nodes on the two end sections of the beam are both kinematically constrained to the reference points located at the geometric centers of the two sections, respectively. One reference point at $x = 0$ is overall clamped in displacements and rotations. The other reference point at $x = l$ is applied with rotation θ_x (θ_1 in VABS coordinate convention). These boundary conditions and constraints approximate a uniformly distributed twisting curvature κ_x (κ_1 in VABS coordinate convention). The reaction twisting moment M_x (M_1 in VABS coordinate convention) on reference point at $x = l$ is requested from the solution data base. The twisting curvature of the 3D beam is approximately estimated by

$$\kappa_x = \frac{\theta_x}{l} \tag{59}$$

This twisting curvature is input into VABS to obtain the nonlinear beam twisting constitutive curve. This curve is compared with the reaction twisting moment and curvature data reported from the 3D FEA, as shown in Fig. 8.

The discrepancies between VABS and 3D FEA in Figs. 7 and 8 are mainly caused by the boundary effects due to the kinematical couplings on the end sections. The approximations of the bending and the twisting curvatures, κ_1 and κ_2, in these examples may also induce the differences. However, the agreement is good considering that the computational cost is dramatically reduced.

3.2. Three-dimensional stresses

From 3D FEA of simple tension, coordinates and stress components (values are measured in lamina coordinate) on the integration points located at the beam axial coordinate $X = 0.09975$ m are reported. The contour plots of this sectional stress fields are compared to the field results obtained from VABS for the final incremental step, as shown in Figs. 9–14 for σ_{11}, σ_{12}, σ_{13}, σ_{22}, σ_{23}, and σ_{33}, respectively. Note that in 3D FEA model the reference coordinate originates from the left-bottom corner of the section. And in VABS the reference coordinate originates from the sectional geometric center. Good agreement can be found between VABS and 3D FEA. From Figs. 11, 13, and 14, it can be seen that highly concentrated stress field occurs at the interfaces between two dissimilar layers along the free edges. The stress fields are localized within the boundary region and exhibit steep gradients with a rapidly decaying behavior towards the inner laminate region. This is the so-called free-edge effect [26,27]. To further investigate this phenomenon, stress data along the free-edges and the interface boundaries will be plotted in the next section. For the sake of space, VABS predictions and the 3D FEA results of the local stress fields due to bending and twisting actions are compared and documented in the Appendix.

3.3. Mesh dependency

In this section, a mesh dependency study will be presented. The denotation of the meshing scheme is $4 \times m \times n$, where m denotes the inner-layer number of mesh divisions through the thickness, and n denotes the transverse number of mesh divisions for all layers. For example, the meshing scheme used in the previous section is $4 \times 9 \times 36$ as shown in Fig. 15(a). For comparison purpose, in mesh $4 \times 4 \times 16$, the mesh division of each edge is in the double-bias pattern in order to keep the same element size as in the mesh $4 \times 9 \times 36$ within the boundaries of the dissimilar layers and the free edges. As shown in Fig. 15(b), the layer-wise through-thickness bias ratio is 3.5, and the transverse bias ratio is 4.1066. In other schemes, the divisions are evenly spaced. Other than $4 \times 9 \times 36$ and $4 \times 4 \times 16$, the other meshing schemes analyzed by VABS are $4 \times 100 \times 36$, $4 \times 200 \times 36$, $4 \times 300 \times 36$, $4 \times 400 \times 36$, $4 \times 500 \times 36$, $4 \times 600 \times 36$, $4 \times 700 \times 36$, $4 \times 800 \times 36$, $4 \times 9 \times 400$, $4 \times 9 \times 800$, $4 \times 9 \times 1200$, $4 \times 9 \times 1600$, $4 \times 9 \times 2000$, $4 \times 9 \times 2400$, $4 \times 9 \times 2800$, and $4 \times 9 \times 3200$. The 3D stress fields converge at

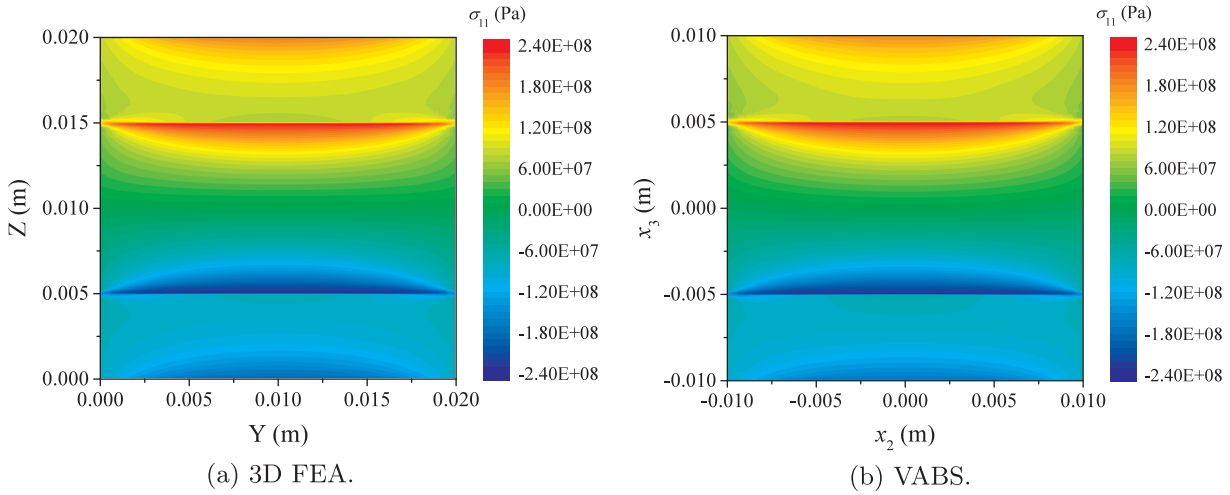

Fig. 26. Comparison of stress σ_{11} contour plots at $\kappa_2 = 2.0$ rad/m.

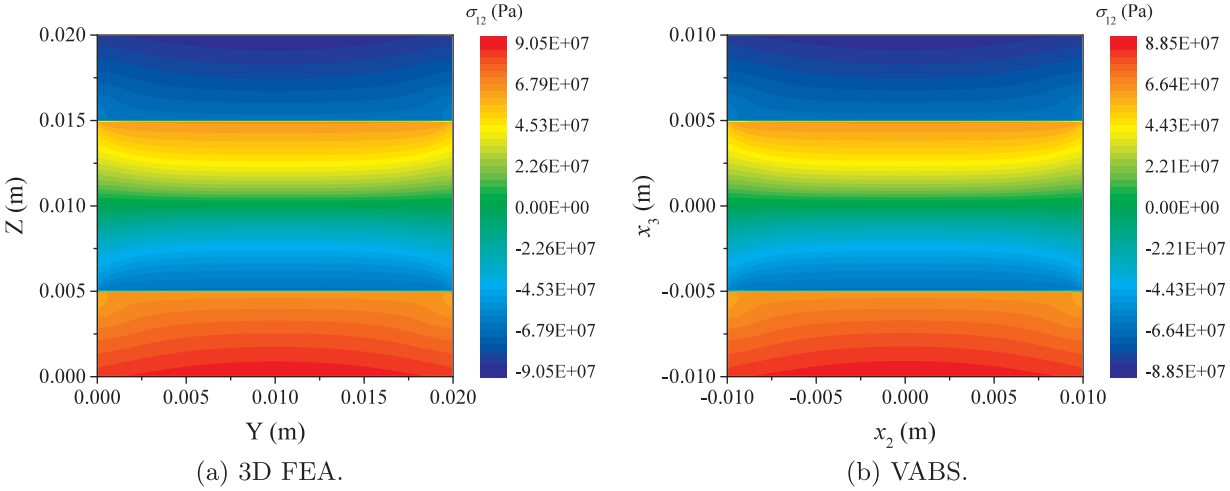

Fig. 27. Comparison of stress σ_{12} contour plots at $\kappa_2 = 2.0$ rad/m.

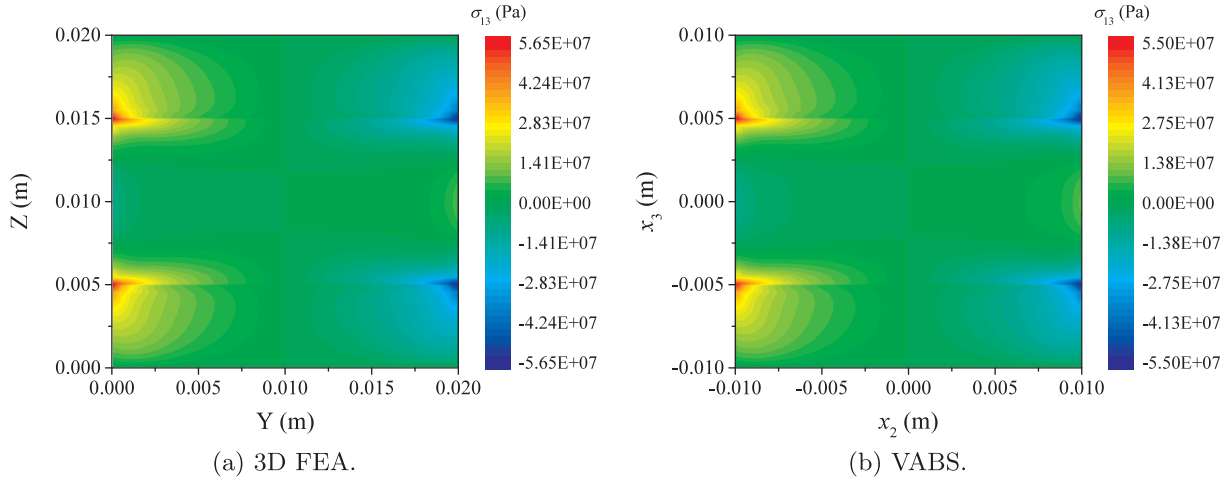

Fig. 28. Comparison of stress σ_{13} contour plots at $\kappa_2 = 2.0$ rad/m.

meshing schemes 4 × 800 × 36 and 4 × 9 × 3200 which are not considered in 3D FEA because of the prohibitive computational cost. The computation aspects of VABS and 3D FEA with meshing scheme 4 × 9 × 36 are compared in Table 1.

For comparison, the coordinates of the integration point data from Abaqus 3D FEA are transformed into the beam sectional triad. For the sake of space, among the meshing schemes denser than 4 × 9 × 36, only 4 × 100 × 36, 4 × 800 × 36, 4 × 9 × 400, and 4 × 9 × 3200 are plotted in Figs. 16–21. Between two dissimilar layers along the free edges, mesh 4 × 800 × 36 and 4 × 9 × 3200 predicts much higher resolutions of stress fields. In Fig. 16(a), σ_{11} along the boundary of dissimilar layers predicted by mesh 4 × 800 × 36 and 4 × 9 × 3200 is

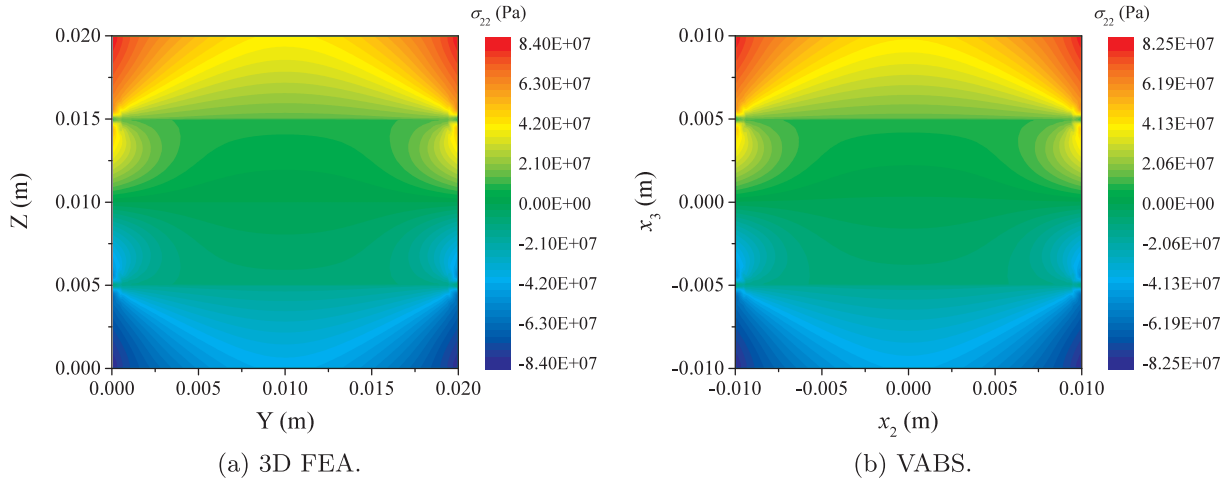

Fig. 29. Comparison of stress σ_{22} contour plots at $\kappa_2 = 2.0$ rad/m.

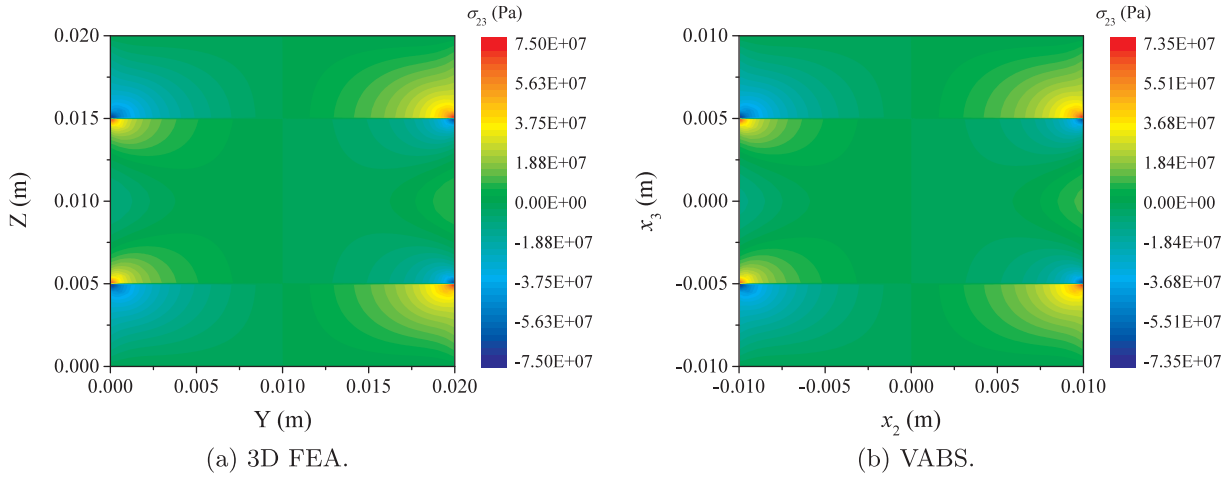

Fig. 30. Comparison of stress σ_{23} contour plots at $\kappa_2 = 2.0$ rad/m.

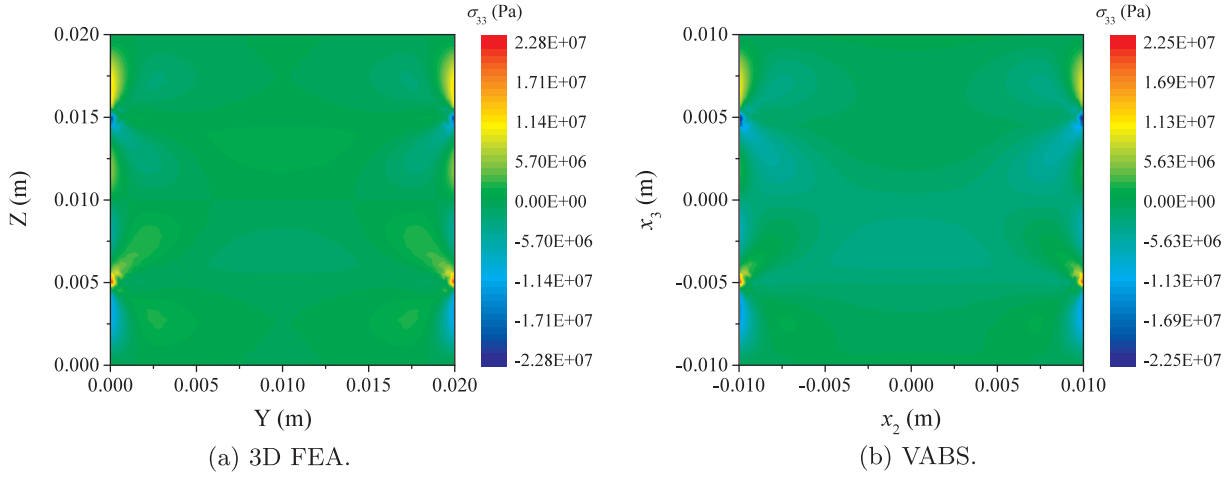

Fig. 31. Comparison of stress σ_{33} contour plots at $\kappa_2 = 2.0$ rad/m.

much larger than predictions from other meshing schemes. σ_{11}, σ_{22}, and σ_{12} predicted by mesh 4 × 9 × 3200 converge to be continuous when x_2 is bigger than 0.008 m or smaller than −0.008 m, as shown in Figs. 16(b), 17(b), and 18(b). From Figs. 19–21, it can be seen that the free-edge effects of σ_{33}, σ_{13}, and σ_{23} have relatively minor mesh dependencies. The agreements between VABS and 3D FEA data of mesh 4 × 4 × 16 and mesh 4 × 9 × 36 are excellent. It is worth to note that the intrinsic semi-analytical feature of VABS enables it to obtain such a high fidelity comparable to 3D FEA with the tremendously reduced computational time cost.

The global beam behavior predictions are relatively mesh-independent. As shown in Table 2, VABS converges faster than 3D FEA does at high loading magnitudes and keep stable when the mesh contains more than 14,400 elements.

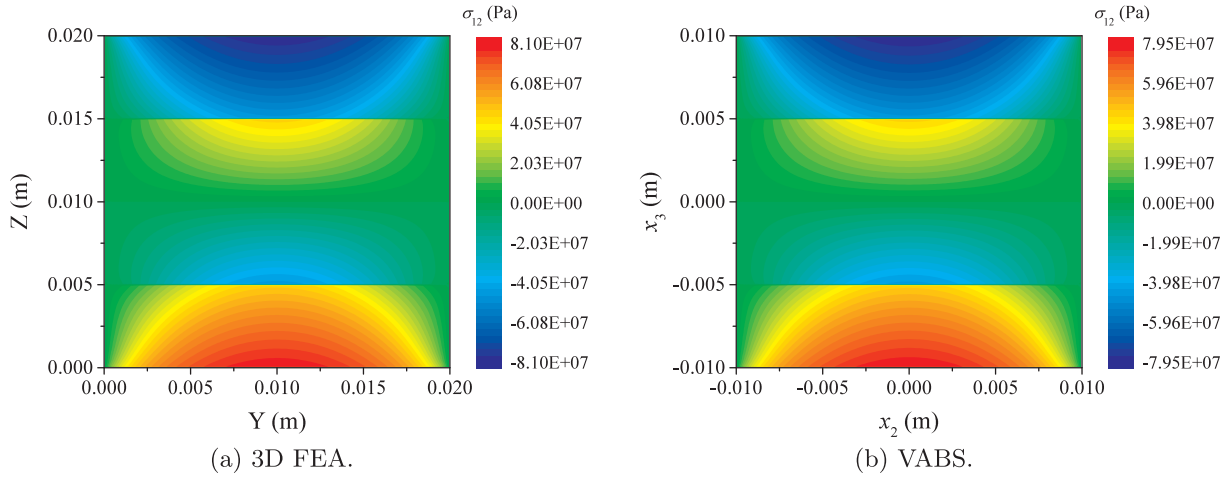

Fig. 32. Comparison of stress σ_{12} contour plots at $\kappa_1 = 2.0$ rad/m.

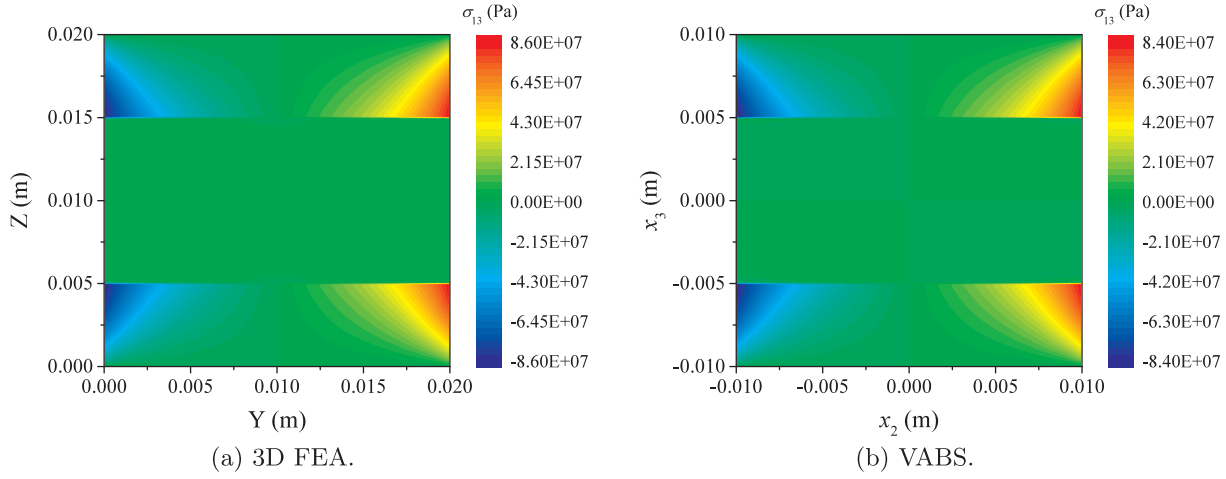

Fig. 33. Comparison of stress σ_{13} contour plots at $\kappa_1 = 2.0$ rad/m.

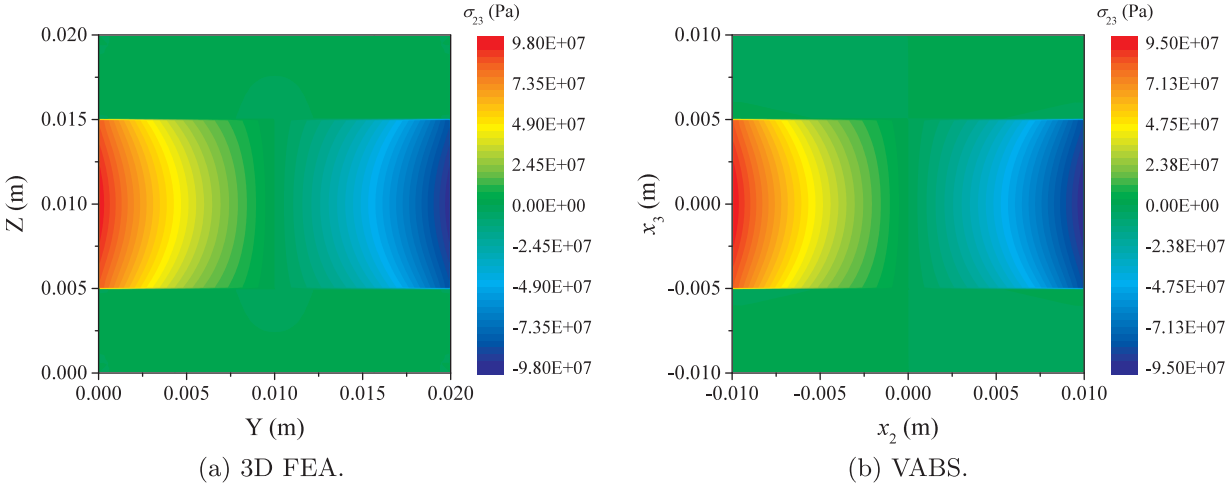

Fig. 34. Comparison of stress σ_{23} contour plots at $\kappa_1 = 2.0$ rad/m.

3.4. Coupon performance

Mechanical properties of a material can be measured from loaded coupons which are in fact structures. Then structural models are used to decipher the material properties from the coupon measurements. For example, to calibrate the in-plane shear response of a polymer matrix composite, slender coupons made by ± 45° laminae are loaded with force F_1 in the beam axial direction. The in-plane shear stress is calculated by $\sigma_{12} = \frac{F_1}{2A}$ where A is the beam cross-sectional area. In-plane responses under such a loading are measured from the beam coupon, and the in-plane shear strain is obtained by $\varepsilon_{12} = \frac{\varepsilon_x - \varepsilon_y}{2}$. This methodology is created based on the Classical Laminate Plate Theory (CLPT). Based on the plane stress assumption, the material constitutive law is reduced to

$$\begin{bmatrix} \varepsilon_{11} \\ \varepsilon_{22} \\ 2\varepsilon_{12} \end{bmatrix} = \begin{bmatrix} \frac{1}{E_1} & -\frac{\nu_{21}}{E_2} & 0 \\ -\frac{\nu_{12}}{E_1} & \frac{1}{E_2} & 0 \\ 0 & 0 & \frac{1}{G_{12}} + \frac{\sigma_{12}^2}{X_{12}} \end{bmatrix} \begin{bmatrix} \sigma_{11} \\ \sigma_{22} \\ \sigma_{12} \end{bmatrix} \tag{60}$$

The ± 45° beam coupon is recommended by the literature [28,29] due to its simplicity, reproducibility, and economy. Several limitations are applied on the coupon design in order to keep the acceptable accuracy. Petit [30] pointed out that small positive or tensile strains exist in addition to the relatively large shear strains in the principal direction of the laminae. Consequently, tensile stress should exist in the longitudinal and transverse directions of the laminae, which will be proved with examples in the present work. Rosen [31] considered the free edge effect in the choice of the specimen width. Hahn [32] highlighted that the layers should be arranged as homogeneous as possible to obtain the acceptable results. He also claimed that $\sigma_{12} = \frac{F_1}{2A}$ was valid only if the shear and extension was not coupled.

The present beam model is used to investigate such a material calibration method. The first goal is to exam the assumptions and the limitations. And the second goal is to find out if the assumptions made in the calibration are valid when the calibrated material properties are utilized to predict the structural behaviors. The cross-sectional schematics of the virtual beam coupons are listed in the following

- Thick Square: The geometry of Fig. 15 with layup $[\pm 45_{37}]_s$ is considered. There are 148 plies and the single ply thickness is 1.351315×10^{-4} m. This example represents an inhomogeneous layup.
- Thick Circular: A tubular cross section of Fig. 22 with layup $[\pm 45_{37}]_s$ is considered. There are 148 plies and the single ply thickness is 1.351315×10^{-4} m. This example represents an inhomogeneous layup and also the shear-extension coupling.
- Thin Rectangle: A very thin layup $[\pm 45]_s$ is considered. The single ply thickness is 1.33×10^{-4} m. The width of the cross section is 0.02 m.
- Thin Circular: A very thin tube with layup $[\pm 45]_s$ is considered. The single ply thickness is 1.33×10^{-4} m. The outmost radius is 0.075 m.
- ASTM D3518: A real coupon cross-sectional geometry with layup $[(+45/-45)_4]_s$ is considered. There are 16 plies and the single ply thickness is 1.32775×10^{-4} m. The width of the cross section is 0.02465 m.
- CLPT: The above five examples are recreated in terms of using shell element (S4R) in Abaqus and the UMAT subroutine is used to apply the in-plane nonlinear shear constitutive law in Eq. (60).

Extensional displacement boundary conditions are applied on these virtual coupons. The predicted constitutive laws are plotted in Fig. 23. All of the five models based on CLPT predict the same result. In light of this fact, instead of plotting multiple overlapped curves, only one curve representing the five cases is plotted in Fig. 23 and marked by the legend CLPT. VABS – Thin Rectangle, VABS – Thin Circular, and VABS – ASTM D3518 agree with CLPT, while VABS – Thick Square and VABS – Thick Circular coupons deviate from CLPT. It is worth to notice that in the VABS – Thick Circular case, there is a coupling between the extension and the twisting. In light of this, a twisting moment is also predicted under the axially extensional displacement boundary conditions. This coupling behavior reduces to a negligible value along with the increasing of the radius-thickness ratio in the VABS – Thin Circular case.

The 3D stress fields of the ASTM D3518 virtual coupon predicted by VABS are plotted in Fig. 24. Firstly, the plane stress assumption is valid only if the layer is arranged as homogeneous as possible, and the layer width is large enough compared to the layer thickness. In this situation, the free-edge stress will be confined in a relatively small cross-sectional area so that its effects on the global force-displacement law can be reasonably neglected. As shown in Fig. 25, the in-plane stress components (from the location centered in the cross section) predicted from VABS – ASTM D3518 are compared to the in-plane stress values predicted by CLPT. The agreement is good. Under the in-plane shear nonlinearity, σ_{11} and σ_{22} are also in nonlinear relations with respect to the beam axial strain γ. Secondly, the plane stress assumption made in a calibration study is not adaptable in the structural simulation when the layers are not arranged as homogeneous as possible, or the width is not large enough compared to the thickness, for example, the case of VABS – Thick Square. Although the plane stress assumption is successful in some specific scenarios, the out-of-plane stresses will become critical when the damage and the delamination are considered.

4. Conclusions

The present theory provides an efficient high-fidelity approach for general predictions of nonlinear shear constitutive laws of composites in beams. By comparison with the predictions from 3D FEA, the nonlinear 1D constitutive relations and 3D stress fields including the free-edge effects are proven to be rigorously captured by the present theory and the computational cost is effectively reduced. Limitations of using the plane stress assumption to calibrate the nonlinear material model is examined. The results show that using the 1D beam constitutive laws predicted by VABS the nonlinear 3D material models can be economically calibrated by data-matching the experimental measurements from slender coupons.

Acknowledgements

This research is supported, in part, by the Army Vertical Lift Research Center of Excellence at Georgia Institute of Technology United States and its affiliate program through a subcontract at Purdue University United States. The views and conclusions contained herein are those of the authors and should not be interpreted as necessarily representing the official policies or endorsement, either expressed or implied, of the funding agency.

Appendix A. Local stress fields of bending and twisting examples

Consider the bending deformation. The stresses predicted by VABS and 3D FEA are contour-plotted and compared in Figs. 26–31. For the twisting example, nontrivial stresses under twisting are plotted in Figs. 32–34. The kinematical couplings on the beam end sections and the approximations of κ_1 and κ_2 in 3D FEA cause the differences. However, good agreement between VABS and 3D FEA can be seen from the plots.

Appendix B. Supplementary material

Supplementary data associated with this article can be found, in the online version, at http://dx.doi.org/10.1016/j.engstruct.2017.10.051.

References

[1] Weinberg M. Shear testing of neat thermoplastic resins and their unidirectional graphite composites. Composites 1987;18(5):386–92. http://dx.doi.org/10.1016/0010-4361(87)90363-6.

[2] Hahn HT, Tsai SW. Nonlinear elastic behavior of unidirectional composite laminae. J Compos Mater 1973;7(1):102–18. http://dx.doi.org/10.1177/002199837300700108.

[3] Chang F-K, Scott RA, Springer GS. Failure strength of nonlinearly elastic composite laminates containing a pin loaded hole. J Compos Mater 1984;18(5):464–77. http://dx.doi.org/10.1177/002199838401800506.

[4] Chang F-K, Chang K-Y. A progressive damage model for laminated composites containing stress concentrations. J Compos Mater 1987;21(9):834–55. http://dx.doi.org/10.1177/002199838702100904.

[5] Ramberg W, Osgood WR. Description of stress-strain curves by three parameters. Tech rep 902. National Advisory Committee For Aeronautics; 1943.

[6] Pinho ST. Modelling failure of laminated composites using physically-based failure models [Ph.D. thesis]. Imperial College London (University of London); 2005.

[7] Donadon MV, Iannucci L, Falzon BG, Hodgkinson JM, de Almeida SFM. A progressive failure model for composite laminates subjected to low velocity impact damage. Comput Struct 2008;86(11):1232–52. http://dx.doi.org/10.1016/j.compstruc.2007.11.004.

[8] Lomakin EV, Fedulov BN. Nonlinear anisotropic elasticity for laminate composites. Meccanica 2015;50(6):1527–35. http://dx.doi.org/10.1007/s11012-015-0104-5.

[9] He Y. Matrix-dominated constitutive laws for composite materials [Ph.D. thesis]. Georgia Institute of Technology; 8 2010.

[10] ASTM. Standard test method for in-plane shear response of polymer matrix composite materials by tensile test of a ± 45° laminate. ASTM D3518/D3518 94. http://dx.doi.org/10.1520/D3518_D3518M.

[11] Carrera E, Giunta G, Petrolo M. Beam structures: classical and advanced theories. John Wiley & Sons; 2011.

[12] Danielson DA, Hodges DH. Nonlinear beam kinematics by decomposition of the rotation tensor. J Appl Mech—Trans ASME 1987;54(2):258–62. http://dx.doi.org/10.1115/1.3173004.

[13] Hodges DH. A mixed variational formulation based on exact intrinsic equations for dynamics of moving beams. Int J Solids Struct 1990;26(11):1253–73. http://dx.doi.org/10.1016/0020-7683(90)90060-.

[14] Hodges DH, Atilgan AR, Cesnik CES, Fulton MV. On a simplified strain energy function for geometrically nonlinear behaviour of anisotropic beams. Compos Eng 1992;2(5):513–26. http://dx.doi.org/10.1016/0961-9526(92)90040-D.

[15] Yu W, Hodges DH. Elasticity solutions versus asymptotic sectional analysis of homogeneous, isotropic, prismatic beams. J Appl Mech—Trans ASME 2004;71(1):15–23. http://dx.doi.org/10.1115/1.1640367.

[16] Yu W, Hodges DH, Ho JC. Variational asymptotic beam sectional analysis—an updated version. Int J Eng Sci 2012;59:40–64. http://dx.doi.org/10.1016/j.ijengsci.2012.03.006.

[17] Lee C-Y, Yu W. Variational asymptotic modeling of composite beams with spanwise heterogeneity. Comput Struct 2011;89(15):1503–11. http://dx.doi.org/10.1016/j.compstruc.2011.04.015.

[18] Berdichevsky VL. Variational principles of continuum mechanics, 1st ed. La Vergne (TN, USA): Springer-Verlag; 2009. p. 243–69 [chapter 5]. http://dx.doi.org/10.1007/978-3-540-88467-5.

[19] Popescu B, Hodges DH. Asymptotic treatment of the trapeze effect in finite element cross-sectional analysis of composite beams. Int J Non-linear Mech 1999;34(4):709–21. http://dx.doi.org/10.1016/S0020-7462(98)00049-3.

[20] Jiang F, Yu W, Hodges DH. Analytical modeling of trapeze and Poynting effects of initially twisted beams. J Appl Mech – Trans ASME 2015;82(6):061003. http://dx.doi.org/10.1115/1.4030362.

[21] Jiang F, Yu W. Nonlinear variational asymptotic sectional analysis of hyperelastic beams. AIAA J 2015;54(2):679–90. http://dx.doi.org/10.2514/1.J054334.

[22] Anand L. On H. Hencky's approximate strain-energy function for moderate deformations. J Appl Mech—Trans ASME 1979;46(1):78–82. http://dx.doi.org/10.1115/1.3424532.

[23] Anand L. Moderate deformations in extension-torsion of incompressible isotropic elastic materials. J Mech Phys Solids 1986;34(3):293–304. http://dx.doi.org/10.1016/0022-5096(86)90021-9.

[24] Engelstad SP, Stover RJ, Action JE. Air vehicle integration and technology research (AVIATR) task order 0037: assessment, qualification and benefits of applying damage tolerant design principles to advanced composite aircraft structure. Tech rep AFRL-RQ-WP-TR-2-15-0068. Wright-Patterson Air Force Base (Ohio, USA): Air Force Research Laboratory, Aerospace Systems Directorate; February 2015.

[25] ABAQUS Theory Manual. Dassault Systèmes Simulia Corp.; 2011.

[26] Pipes RB, Pagano NJ. Interlaminar stresses in composite laminates under uniform axial extension. Mechanics of composite materials Springer; 1994. p. 234–45. http://dx.doi.org/10.1007/978-94-017-2233-9_19.

[27] Peng B, Goodsell J, Pipes RB, Yu W. Generalized free-edge stress analysis using mechanics of structure genome. J Appl Mech 2016;83(10):101013. http://dx.doi.org/10.1115/1.4034389.

[28] Chiao C, Moore R, Chiao T. Measurement of shear properties of fibre composites: Part 1. Evaluation of test methods. Composites 1977;8(3):161–9. http://dx.doi.org/10.1016/0010-4361(77)90011-8.

[29] Lee S, Munro M. Evaluation of in-plane shear test methods for advanced composite materials by the decision analysis technique. Composites 1986;17(1):13–22. http://dx.doi.org/10.1016/0010-4361(86)90729-9.

[30] Petit P. A simplified method of determining the inplane shear stress-strain response of unidirectional composites. In: Composite materials: testing and design. ASTM International; 1969. http://dx.doi.org/10.1520/STP49808S.

[31] Rosen BW. A simple procedure for experimental determination of the longitudinal shear modulus of unidirectional composites. J Compos Mater 1972;6(4):552–4. http://dx.doi.org/10.1177/002199837200600310.

[32] Hahn HT. A note on determination of the shear stress-strain response of unidirectional composites. J Compos Mater 1973;7(3):383–6. http://dx.doi.org/10.1177/002199837300700308.